



Original Paper

Physical Properties, Pore-Throat Structure, Fractal Characteristics and Their Effects on the Gas-Bearing Capacity of Tight Sandstone: A Case Study from the Northern Tianhuan Depression, Ordos Basin, China

Hang Cui,^{1,2} Shifa Zhu,^{1,2,5} Jianpeng Wang,³ Yang Gao,⁴ Chaofan Wan,^{1,2} and Huan Tong^{1,2}

Received 2 August 2021; accepted 24 March 2022
Published online: 20 April 2022

In this study, various testing methods were used to analyze the mineral characteristics, reservoir storage types and pore-throat network characteristics of the Permian tight sandstone in the Upper Paleozoic of the Ordos Basin. A fractal method was applied to evaluate the reservoirs' microscopic heterogeneity. According to the results, the storage space of the sandstone reservoir is predominantly intra-granular dissolution pores and kaolinite inter-crystalline pores, while primary pores and inter-granular dissolution pores form secondary spaces with low concentration and poor homogeneity of pore-throat size distribution. All samples were divided into four categories on account of porosity (ϕ), pore-throat size distribution and multifractal dimensions (D): Type A ($\phi > 10\%$) consisted mainly of macropores; Type B ($\phi < 6\%$, consisting mainly of transitional pores and micropores); Type C₁ ($6\% < \phi < 10\%$, consisting mainly of mesopores, $D > 2.45$); and Type C₂ ($6\% < \phi < 10\%$, consisting mainly of mesopores, $D < 2.45$). In general, the piecewise fractal dimension was associated with porosity, different pore size ranges and the pore-throat parameters. Between Types A and B samples, porosity and pore size distribution were the major controlling factors on gas-bearing capacity, while the microscopic pore-throat heterogeneity had little influence. However, the microscopic pore-throat heterogeneity had a significant effect on gas-bearing capacity in Types C₁ and C₂ samples. This study discusses the applicable pore size range for fractal analysis of tight sandstone based on fine reservoir division and provides a novel idea for the control of the microscopic pore-throat heterogeneity on gas-bearing capacity in tight sandstone.

KEY WORDS: Microscopic heterogeneity, Fractal dimension, Physical properties, Gas-bearing capacity, Tight gas sandstone.

¹State Key Laboratory of Petroleum Resources and Prospecting, China University of Petroleum (Beijing), Beijing 102249, China.

²College of Geosciences, China University of Petroleum, Beijing 102249, China.

³School of Earth and Environmental Sciences, University of Manchester, Manchester M13 9PL, UK.

⁴PetroChina Research Institute of Petroleum Exploration & Development, Beijing 100083, China.

⁵To whom correspondence should be addressed; e-mail: sfzhu@cup.edu.cn

INTRODUCTION

Tight sandstones are important to the development of natural gas reserves and consequently for energy supply and are thereby an important focus of current research (Mcglade et al., 2013; Lai et al.,

2018; Zhu et al., 2020). Tight sandstones are those with in situ permeability and porosity lower than 1 mD¹ and 10%, respectively (Zou et al., 2013). In China, more than 10 basins, such as Ordos, Qaidam, Songliao, Bohai Bay, Tarim and Junggar, possess the right geologic conditions for the formation of tight gas and are ideal areas for prospecting (Jia et al., 2012). Of these, the Ordos basin is comprised of a layer of widely distributed tight sandstone reservoirs formed during the Upper Paleozoic (Zou et al., 2013). This set of tight sandstone is characterized by a complex macro-scale gas–water distribution accompanied by a complex micro-scale pore-throat structure and high heterogeneity in pore morphology (Wang et al., 2017). The intricate geometry found with the pore network controls not only the reservoir quality, but also hydrocarbon accumulation. Therefore, clarifying the micro-structure in the pore network is crucial to the understanding of enrichment regularity of tight gas.

Measurement techniques for 2D or 3D pore-throat structure have developed rapidly, undergoing continuous improvement to better detect and characterize pore-throat structures (Ougier-Simonin et al., 2016). These measurement techniques characterize pore type, pore morphology and pore size range accurately and quantitatively, but they cannot characterize the microscopic pore-throat heterogeneity quantitatively. Reservoir heterogeneity may occur in various extents (nanoscale or even several hundred-meter scale) (De Ros, 1998; Morad et al., 2010). Although the physical properties in tight sandstone are not of the same quality as those found in conventional sandstone, tight sandstone still shows high heterogeneity leading to important differences in hydrocarbon migration and accumulation in reservoirs with similar physical properties (Shanley & Cluff, 2015; Zha et al., 2018; Zhu et al., 2020). Grasping the pore-throat characteristics is conducive to a better understanding of the connectivity and adsorption capacity of pores, which are key to any discussion on reservoir heterogeneity.

Mandelbrot et al. (1984) proposed the fractal theory to overcome the shortcomings of Euclidean geometry in describing special geometrical structures. In recent years, it has increasingly been applied to characterize the heterogeneity of complex geometry with a large degree of success (Schlueter et al., 1997; Cai et al., 2010; Huang et al., 2017). Previous research has shown that the pore-throat

network present within rock has self-similar characteristics, and the degree of microscopic pore-throat heterogeneity can be described quantitatively by fractal dimension (denoted as D) (Pfeifer, 1984). In addition, a complex pore-throat structure can be divided into several segments based on the multi-fractal theory, further ensuring the accuracy of pore-throat heterogeneity calculations (Wu et al., 2019). Values of D can be calculated with the aid of nuclear magnetic resonance (NMR), nitrogen adsorption or high-pressure mercury injection (HPMI) experiment, and the effectiveness of applying fractal geometry to rock pore-throat structure is widely supported (Schlueter et al., 1997; Huang et al., 2017; Li et al., 2017; Sun et al., 2019; Nie et al., 2021). However, there is a fundamental problem in the fractal study of pore-throat structure. Most previous researches that utilized this technique have failed to demonstrate whether values of D could effectively identify reservoirs or even oil and gas relationships. Additionally, there is lack of research on the applicable pore size range of fractal theory in tight sandstone.

Tight sandstone gas is characterized by unclear trap boundary, close contact between source and reservoir, and continuous hydrocarbon accumulation over large areas (Zou et al., 2013). Factors controlling prolific gas production from tight sandstone reservoirs are significantly different from those in conventional sandstone (Shanley et al., 2004). Generally, multi-factors such as pore-throat structure, charging pressure, water saturation, formation pressure, stress-sensitivity, etc., jointly control the occurrence and distribution of tight gas (Nie et al., 2016, 2021; Huang et al., 2017). However, there are specific characteristics related to tight gas accumulation mechanisms and controlling factors in the Tianhuan Depression, Ordos Basin. Previous research has shown that the Tianhuan Depression has long been in a relatively stable tectonic setting. The condition of hydrocarbon generation intensity and gas charging mode is almost the same in the He 8 and Shan 1 Members in the study area (Zhang et al., 2017). Furthermore, there is no evidence of abnormal pressure in the Tianhuan Depression. Therefore, reservoir physical property and pore-throat structure have an important controlling effect on tight gas formation. He 8 and Shan 1 Members in the Tianhuan Depression has become a 'natural laboratory' to study the reservoir characteristics and single-factor controls on gas-bearing capacity.

¹ * 1 mD = 1 millidarcy = $0.986923 \times 10^{-15} \text{ m}^2$.

Under this geological background and employing a variety of qualitative and quantitative methods (scanning electron microscope (SEM), HPMI, laser confocal microscopy and CT) and oil-gas interpretation data, this article focuses on the characteristics of reservoir pore-throat micro-structure and discusses the applicable pore size range for fractal analysis of tight sandstone. Previous interpretations have focused on microscopic pore-throat heterogeneity inhibiting hydrocarbon accumulation. However, this present research found the opposite relationship, explaining it in terms of the chronological order between hydrocarbon accumulation and reservoir densification. Therefore, this provided a novel idea for the control of microscopic pore-throat heterogeneity on gas-bearing capacity in tight sandstone.

GEOLOGICAL SETTING

The Ordos Basin is a multi-cycle craton basin and it covers $250,000 \times 10^4 \text{ km}^2$ (Hanson et al., 2007; Zhu et al., 2017). It has the highest gas reserves in China, and it ranks fourth as a petroleum resource. The basin is a vast area south of the Yinshan Mountains, north of the Qinling Mountains, east of the Helan Mountains and west of the Luliang Mountains. The basin can be divided into six tectonic units, of which the Tianhuan Depression (the study area) is situated in the western part of the basin, with nearly north-south orientation (Li et al., 2008; Zhu et al., 2020). Its east wing is broad, while the west wing is steep and narrow, connecting to the Yishaan Slope and the Western Thrust Belt, which comprises an important part of the basin (Fig. 1).

The basin floor is composed of Archean and Proterozoic metamorphic rock series. There are five stages in the overlying sedimentary cap: (1) a Paleozoic aulacogen stage, during which the basin foundation was formed; (2) a sublittoral platform stage in Early Paleozoic, during which the basin was mainly marine carbonate deposits with thickness of 400–1000 m; (3) a Late Paleozoic offshore plain stage, which was affected by Hercynian movement, during which the basin was uplifted and the subsidence rate was stable, and coal measures strata and fluvial delta clastic rock were dominant, and the thickness of sedimentary strata was about 1000 m; (4) a Mesozoic inland lacustrine stage, during which the basin underwent a fundamental transformation from marine, transitional to continental facies, and

thereby developing a typical continental clastic sedimentary system; (5) a Cenozoic fault depression stage, during which the whole basin was uplifted under the influence of the Himalayan movement, and a series of small fault depressions were formed in the surrounding area. Except for the missing strata of Lower Carboniferous, Devonian and Silurian in Ordos Basin, the strata of other ages are basically complete. Affected by different tectonic activities, some strata in the basin show false conformity or parallel unconformity relationship.

The Late Carboniferous to Early Permian period in the Ordos Basin was dominated by paralic facies. In the process of transgression and regression, large and exposed coastline areas became swampy sedimentary environments. Combined with gentle topography, lush vegetation, warm and moist climatic conditions and stable subsidence, a wide range of source rocks were formed. Experiment samples were selected from the He 8 and Shan 1 Members of the Middle and Lower Permian in the Upper Paleozoic (Fig. 2). These two members constitute the main gas-bearing formation in the Tianhuan Depression, which developed the typical reservoir of low porosity, low permeability, low pressure and low gas abundance. The overall physical property is below 10% and 1 mD, with the He 8 Member being slightly better than Shan 1 Member (Li et al., 2012). The thickness of the He 8 and Shan 1 Members is 60–80 m and 30–60 m, respectively. The braided river delta and meander river delta with a common provenance area in the north were developed, respectively, during the sedimentary periods of the He 8 and Shan 1 Members in the Tianhuan Depression, and reservoir sand bodies were superimposed and distributed throughout large areas (Zhu et al., 2020).

MATERIALS AND METHODS

Samples and Data Materials

The core sample depths of the He 8 and Shan 1 Members ranged from 3502 to 4469 m. The samples were tested by various analytical techniques, including casting thin sections, SEM, X-ray diffraction and petrophysical property analysis, which focused on observation and analysis of the rock mineral characteristics, reservoir space types and microscopic pore-throat heterogeneity. Based on the test results, 19 samples were selected for HPMI

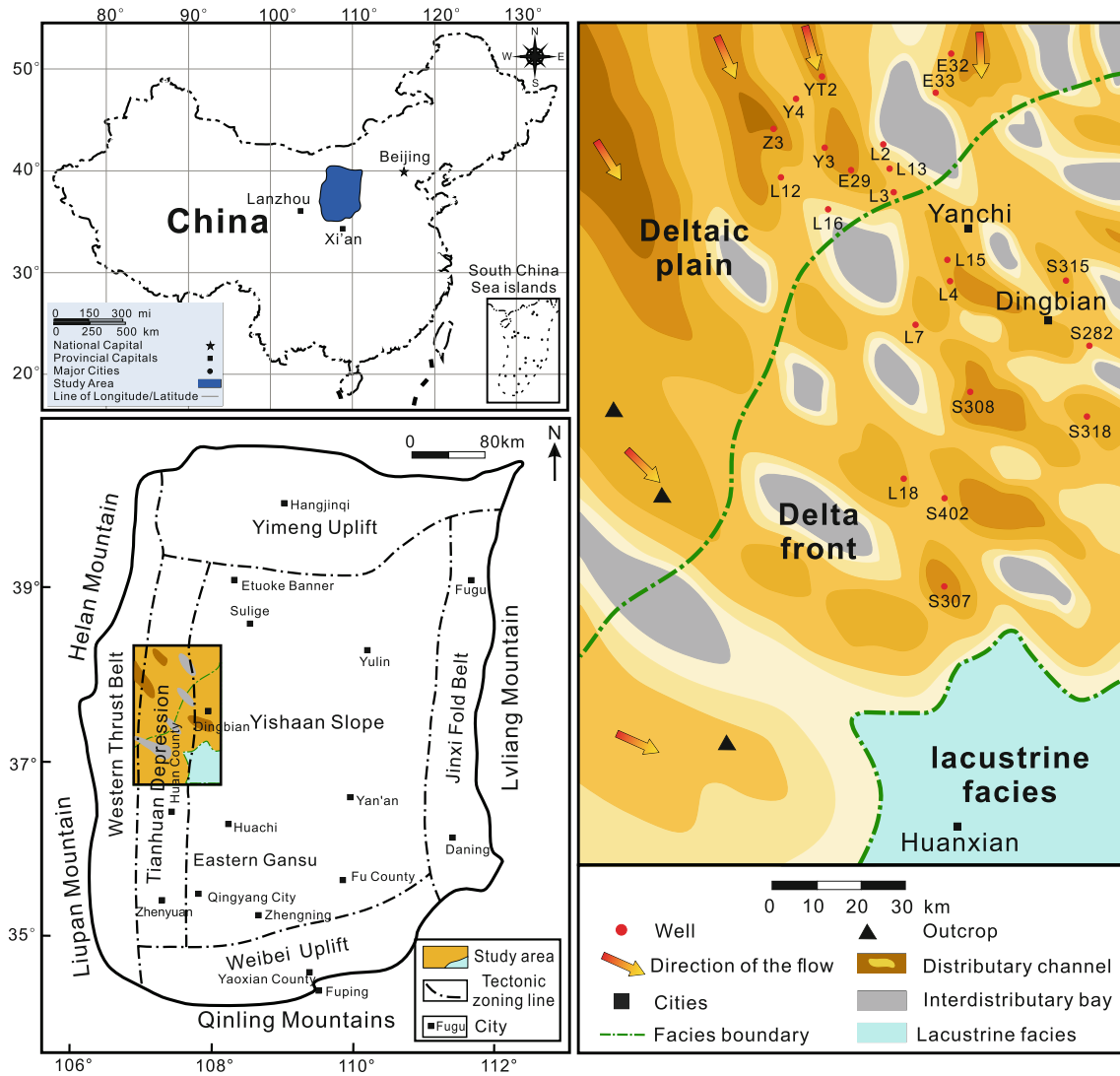


Figure 1. Geological Setting, location and sedimentary facies distribution characteristics of Tianhuan Depression.

analysis, and the values of D of these samples were calculated according to the HPMT parameters. The selected samples were all tight sandstone, as reflected by different gas-bearing capacities (including gas formations, poor-gas formations and dry formations). The purpose of sample selection was to compare physical properties, pore-throat structure, fractal characteristics and their effects on gas-bearing capacity.

In total, 568 thin sections were made for investigating mineralogical characteristics, storage space types and clay growth occurrence and habits. More than half of the thin sections were impregnated with blue epoxy resin to facilitate the deter-

mination of pore size and pore type. The thin section photographs used in this paper were captured by a metallographic microscope BX51 produced by Olympus, with a 12 V/100 W halogen lamp as light source. The optical acquisition system was an Olympus Stream provided by Olympus Soft Imaging Solutions GmbH. The database of rock and mineral compositions to aid identification was provided by CNPC Changqing Oilfield Company.

For further detailed analysis of the microstructure of tight sandstone, 46 samples were collected for microscopic observation using S-4800 SEM equipment. At high acceleration voltage (15 kV), the resolution of a secondary electron image of S-

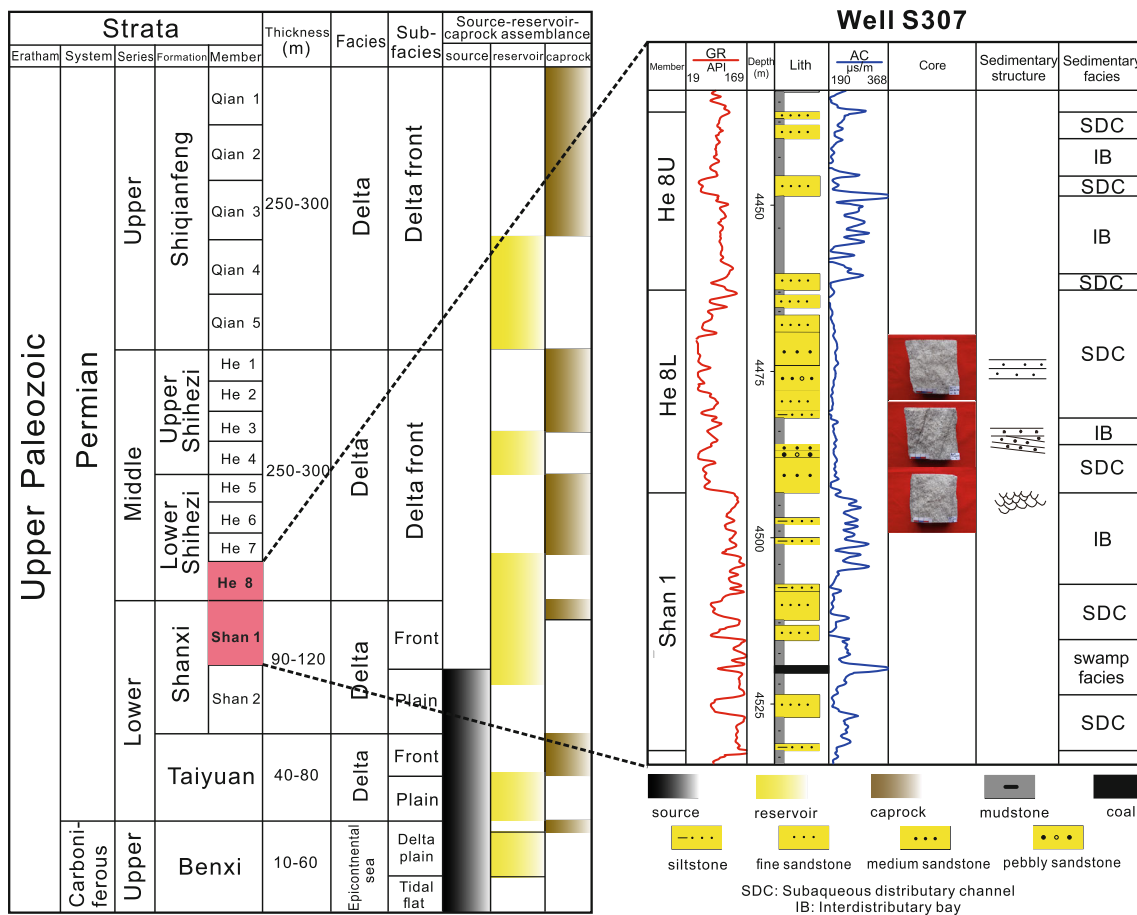


Figure 2. Generalized stratigraphy of the Upper Paleozoic in Ordos Basin and lithological association of the He 8 and Shan 1 Members, based on Well S307.

4800 is 1 nm, and at low acceleration voltage (1 kV), the resolution of a secondary electron image of S-4800 is 2 nm. The magnification ranged from $\times 30$ to $\times 800,000$. An S-4800 combined with an X-ray energy spectrometer can observe sample mineral crystal morphology, and it can be used to perform qualitative and quantitative analysis of micro-composition and element distribution.

Helium porosity and horizontal permeability were obtained by a JS100007 helium porosimeter and a A-10133 gas (nitrogen) permeameter, respectively. The porosity and permeability were measured in accordance with the ‘Standard of the People’s Republic of China’ (GB/T 29172-2012). The database were provided by the CNPC Changqing Oilfield Company.

A YG-97 mercury injection apparatus was used in HPMI experimentation. At room temperature, the mercury injection apparatus pressure range was 0.01–50 MPa, and the pore size test range was 30 nm–600 μm . The YG-97 capacitor mercury

injection apparatus complies with ISO 15901-1:2005 International Standard and GB/T 21650.1-2008 National Standard.

In this study, the interpretation of gas-bearing capacity in the tight sandstone reservoir was based mainly on comprehensive logging evaluation. The gas-bearing capacity was divided into three types: ‘gas formation’, ‘poor-gas formation’ and ‘dry formation’. The comprehensive logging evaluation and identification criteria are shown in Table 1. The evaluation criteria and interpretation results were provided by the CNPC Changqing Oilfield Company.

Fractal Theory

Fractal theory can be applied to study irregular and complex natural phenomena (Mandelbrot et al., 1984). Recent studies have shown that rock pore-throat network, a complex geometry, has self-similar

Table 1. Logging interpretation and gas-bearing capacity evaluation criteria of Shan 1 and He 8 Members in the Tianhuan Depression, Ordos Basin

Logging parameters	Gas-bearing formation		Poor gas-bearing formation		Dry formation
	Gas > Water	Gas ≈ Water	Gas > Water	Gas < Water	
GR	< 45 API	< 65 API	< 65 API	< 65 API	< 85 API
DEN	< 2.65 g/cm ³	< 2.65 g/cm ³	< 2.65 g/cm ³	< 2.65 g/cm ³	> 2.65 g/cm ³
RLLD & AC	log (RLLD) > 6.6 × 10 ⁵ / AC ^{2.215}	log (RLLD) > 8.9 × 10 ⁵ / AC ^{2.29}	log (RLLD) > 6.74 × 10 ⁵ / AC ^{2.254}	log (RLLD) > 5.12 × 10 ⁵ / AC ^{2.227}	log (RLLD) < 5.12 × 10 ⁵ / AC ^{2.227}
RLLD & ILLD	RLLD > -312.5 × ILLD/ RLLD + 275	RLLD > -312.5 × ILLD/ RLLD + 275	RLLD < -312.5 × ILLD/ RLLD + 275	RLLD < -312.5 × ILLD/ RLLD + 275	-

characteristics, and the degree of heterogeneity of rock microscopic pore-throat could be represented quantitatively by D (Pfeifer, 1984). In the rock pore-throat network system, the number of pores $N (> r)$ whose pore-throat size exceeds r can be indicated by Eq. 1 (Mandelbrot et al., 1984):

$$N(>r) = \int_r^{r_{\max}} P(r)dr \propto r^{-D} = \alpha r^{-D} \quad (1)$$

where α is the fractal factor, r represents pore-throat radius (μm), r_{\max} represents maximum pore-throat radius (μm), $P(r)$ represents the distribution function of pore radius and D represents fractal dimension. According to the sphere model and fractal theory (Zhu et al., 2018), the derivatives of both sides of Eq. 1 are taken with respect to r , and Eq. 1 can be converted to:

$$P(r) = \frac{dN(>r)}{dr} = \alpha' r^{-D-1} \quad (2)$$

where α' is a proportional constant and has no effect on the subsequent fractal dimension calculation, which is numerically equal to $-\alpha \times D$. If the geometrical shape of pores in rocks is idealized as a cube, $\alpha = 1$; and, if the geometrical shape is idealized as sphere, $\alpha = 4\pi/3$ (Li et al., 2017). Therefore, total cumulative pore volume V with radius less than r should be represented as:

$$V(<r) = \int_{r_{\min}}^r P(r)\alpha r^3 dr = \alpha''(r^{3-D} - r_{\min}^{3-D}) \quad (3)$$

where r_{\min} represents the radius (μm) of the smallest pore-throat in the sample and α'' is also a proportional constant, which can be eliminated in subsequent calculations, and numerically equals $\alpha'\alpha/(3-D)$. By derivation and calculation, the total pore-throat volume (V_{total}) is:

$$V_{\text{total}} = \alpha''(r_{\max}^{3-D} - r_{\min}^{3-D}) \quad (4)$$

Based on Eqs. 3 and 4, the cumulative pore volume proportion S_w with radius smaller than r is:

$$S_w = \frac{V(<r)}{V} = \frac{r^{3-D} - r_{\min}^{3-D}}{r_{\max}^{3-D} - r_{\min}^{3-D}} \quad (5)$$

Because r_{\min} in the samples is much less than r_{\max} in the pore network, the above equation could be reduced to:

$$S_w = \frac{V(<r)}{V} = \frac{r^{3-D}}{r_{\max}^{3-D}} = \left(\frac{r}{r_{\max}}\right)^{3-D} \quad (6)$$

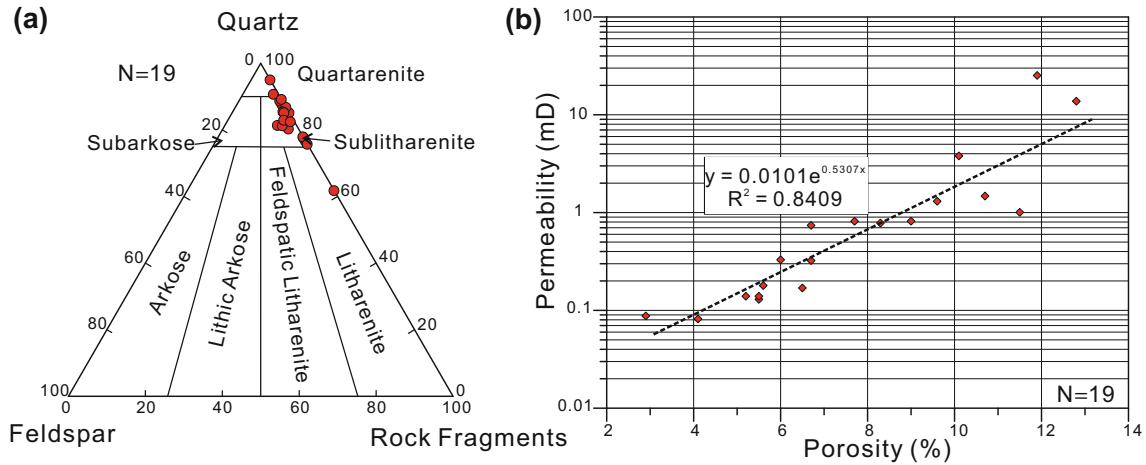


Figure 3. Petrology and reservoir physical properties of tight sandstone reservoirs in the He 8 and Shan 1 Members of Upper Paleozoic. (a) Sandstone-type triangular diagram using the Folk's criteria (1974); (b) Plot of permeability versus porosity for tight sandstone samples in He 8 and Shan 1 Members.

According to Washburn's formula, $p_c = 2\sigma\cos\theta/r$ (Washburn, 1921), it is assumed that the wetting contact angle is independent of pore size (Sun et al., 2019), and Eq. 6 can be converted to:

$$S_w = \left(\frac{p_d}{p_c}\right)^{3-D} \quad (7)$$

where p_d represents the displacement pressure (psi^2) corresponding to the maximum pore radius R_{\max} , σ represents the surface tension of mercury (480 dN/cm) and θ represents the wetting contact angle of mercury (146°). Taking logarithm base 10 of both sides of Eq. 7, we obtain:

$$\log S_w = (D-3)\log p_c - (D-3)\log p_d \quad (8)$$

where S_w represents the wet phase saturation (%) corresponding to mercury pressure p_c .

The slope S can be obtained by linearly fitting the plot of $\log S_w$ versus $\log p_c$ with least square method, and finally, the fractal dimension D is expressed as:

$$D = 3 + S \quad (9)$$

The values of D of porous media vary generally between 2.0 and 3.0 (Broseta et al., 2001). For rock pore-throat structure, the closer the fractal dimension is to 3.0, the more irregular the pore-throat geometry or the rougher the pore surface, while a D close to 2.0 corresponds to more orderly pore-throat structure and a smoother pore surface (Yang et al., 2016). For the fractal analysis of non-homogeneous media, it can be regarded as a set composed of a single D , and piecewise regression can be carried out based on pore size distribution. A rock sample (whose dimension is 1) can be divided into N intervals according to the pore size range. Let the dimension of the i th region be ε_i , and the weighted sum of total fractal dimension is:

$$D_{\text{total}} = \sum_{i=1}^N \varepsilon_i D_i \quad (10)$$

$$\varepsilon_i = \frac{\phi_i}{\phi_{\text{total}}} \quad (11)$$

where D_{Total} represents total D , D_i represents the piecewise D of different pore size ranges, ϕ_i represents the porosity (%) of different pore size ranges, and ϕ_{Total} represents total porosity. Like D_{Total} , D_i also ranges from 2 to 3 and it is a quantitative representation of rock heterogeneity. This method not only ensures accuracy and integrity of the D_{Total} calculation, but it can also reflect accurately the microscopic pore-throat heterogeneity at different scales (Wu et al., 2019).

² * 1 psi = 6.89476 kPa.

RESULTS

Mineralogical Characteristics and Petrophysical Properties

Based on observations from 19 thin sections, He 8 and Shan 1 reservoir rocks were mostly sublitharenite with quartz arenite (Fig. 3a) according to the classification standard of Folk (1974). The mean framework composition was $Q_{84.5}F_{0.9}R_{14.6}$. The detrital mineral was mainly quartz, accounting for 66.9–95.7%. Rock fragments ranged from 4.3 to 33.1%, generally representing high metamorphic rock content, moderate amounts of sedimentary rocks and a small amount of magmatic rock debris. The rock detrital grains were commonly subangular to subrounded and the sorting rank was moderate to high. The authigenic minerals in the study area ranged from 9.0 to 21.0%, including quartz overgrowths, calcite, siderite and clay minerals. The content of clay mineral cements was higher, ranging from 6.0 to 15.0%, with average of 8.9%, including a large proportion of kaolinite, a small amount of illite, and negligible chlorite.

The porosity, permeability, HPMI parameters and rock composition data for the 19 tight sandstone samples are listed in Table 2. The results showed that He 8 and Shan 1 Members in the Tianhuan Depression have poor physical properties and belong to typical tight sandstone. The porosity of all samples ranged from 2.9 to 12.8%, with average of 7.70%, among which those with porosity's ranging from 5 to 9% accounted for more than 60% of all samples. Permeability ranged from 0.08 to 25.30 mD, about 75% of all have permeability of more than 1 mD. Figure 3 illustrates that the tight sandstone porosity and permeability in the study area have strong correlation coefficient R^2 of 0.8409 (Fig. 3b).

Pore Types and SEM Analysis

The rock storage space of tight reservoirs in the Tianhuan Depression can be segmented into four types: (1) intra-granular dissolution pores; (2) inter-crystalline pores of clay minerals; (3) primary residual pores; and (4) inter-granular dissolution pores. These four types of pore space accounted for 37.2, 23.0, 22.5 and 17.3%, respectively, of the total reservoir space. The primary residual inter-granular pore size was relatively large, usually much larger

than 1 μm , but the content was low (Fig. 4a). Due to the high compositional maturity, this type of triangular or polygon shaped pore can be retained under intensive compaction, especially in coarse-grained quartz arenite with weak cementation. The secondary pores were dominated by intra-granular dissolution pores. The lithic dissolution pores, which were honeycombed in shape (Fig. 4b, c, g), were mainly from volcanic debris. The dissolution pore size was limited by debris grain size, which is a good storage space for natural gas. The morphology of inter-granular dissolution pores varied, and the grains were marked by an obviously dissolved edge (Fig. 4d, g). The throats shape resembled a curved sheet, and so sometimes made it difficult to distinguish the primary residual inter-granular pores, but both have an important contribution to storage and seepage capacity (Zhou et al., 2016). Inter-crystalline pores develop mainly within clay minerals (e.g., clay coatings or rims, authigenic kaolinite, illite and I/S), and their inter-crystal microporosity is generally over 50% (Hurst & Nadeau, 1995). The inter-crystalline pores of clay minerals were formed mostly in the late diagenesis. In these clay minerals, such as leaf chlorite and vermiculate kaolinite, inter-crystalline pores developed with small pore sizes, which were dominated by micro-nano-pores, usually about 1 μm –100 nm (Fig. 4e, f, g).

Due to the extremely complex diagenesis, the complexity and connectivity of different pore types can be quite distinct, and even the pore-throat complexity can vary within the same pore type. Although some well-developed intra-granular dissolution pores were limited by grain size, the distribution of pore size was concentrated, with clear and smooth pore edges, and complexity of microscopic pores being relatively low (Fig. 5a, b). However, some clastic grains such as lithic debris and feldspar were replaced by clay minerals during diagenesis, resulting in poor connection or even complete isolation between dissolution pores and the high microscopic pore-throat heterogeneity (Fig. 5c). As high-quality reservoir space, residual inter-granular pores can not only be found with straight edges and regular shapes under SEM and laser confocal observations (Fig. 5d, e, i), but were also observed to be covered or clogged with authigenic clay minerals. The latter may have changed the pore morphology and increased roughness at the pore edges (Fig. 5e, f, i). Inter-crystalline pores with radii of 1 μm –100 nm developed between flaky, needle shaped illite and vermicular kaolinite and were observed very commonly

Table 2. Porosity, permeability, rock composition and gas-bearing capacity of all samples

Sample	Well name	Depth (m)	Porosity (%)	Permeability (mD*)	Detrital composition content (%)			HPMI parameters			Gas-bearing capacity		
					Quartz	Feldspar	Rigid rock debris	ductile rock debris	Maximum mercury saturation (%)	Maximum radius (µm)		Median radius (µm)	Average radius (µm)
1	S282	3808.9	10.1	3.81	86.9	0	7.1	4.8	85.16	2.96	1.44	1.79	Gas
2	S282	3809.6	11.9	25.30	89.1	0	9.1	1.7	96.07	19.30	3.00	9.66	Gas
3	S282	3810.5	12.8	13.80	90.1	0	9.4	0.6	88.21	20.98	1.60	9.56	Gas
4	L2	3773.5	11.5	1.01	71.0	0	4.0	10.0	98.17	3.69	0.52	0.72	Gas
5	L2	3775.5	10.7	1.48	79.0	0	3.0	3.0	96.68	2.45	0.79	0.77	Poor gas
6	Z3	3479.9	5.5	0.13	65.0	0	4.0	12.5	87.63	0.91	0.08	0.21	Dry
7	Z3	3487.6	5.5	0.14	67.5	0	3.0	12.5	86.74	0.91	0.05	0.21	Dry
8	Z3	3489.6	5.6	0.18	68.0	0	3.0	12.5	91.48	0.91	0.05	0.23	Dry
9	Z3	3493.2	5.2	0.14	55.5	0	4.0	23.5	91.35	1.05	0.06	0.22	Dry
10	Z3	3495.2	6.5	0.17	70.0	0	2.5	13.5	97.81	0.92	0.09	0.20	Dry
11	Y2	3703.9	2.9	0.09	76.0	0	4.0	10.0	66.70	0.50	0.01	0.18	Poor gas
12	L15	3837.2	4.1	0.08	83.4	0	3.3	12.2	65.48	0.39	0.01	0.13	Dry
13	S282	3811.4	9.0	0.82	88.4	0	10.5	1.2	85.13	0.96	0.46	0.69	Gas
14	S282	3855.8	9.6	1.31	87.2	0	6.4	5.8	91.58	0.98	0.40	0.64	Gas
15	L3	3984.1	6.7	0.32	73.0	0	3.0	7.0	86.37	1.48	0.16	0.34	Gas
16	L13	3933.5	6.7	0.74	62.0	0	3.0	13.5	93.15	2.47	0.24	0.47	Gas
17	Z3	3499.7	6.0	0.33	76.0	0	4.0	3.0	94.22	1.47	0.41	0.46	Poor gas
18	E29	3762.91	8.3	0.79	84.9	0	7.8	6.7	89.85	2.04	0.77	1.32	Poor gas
19	L13	3863.0	7.7	0.82	78.0	0	2.0	1.5	94.77	3.70	0.84	0.81	Poor gas

*1 mD = 1 millidarcy = 0.986923 × 10⁻¹⁵ m²

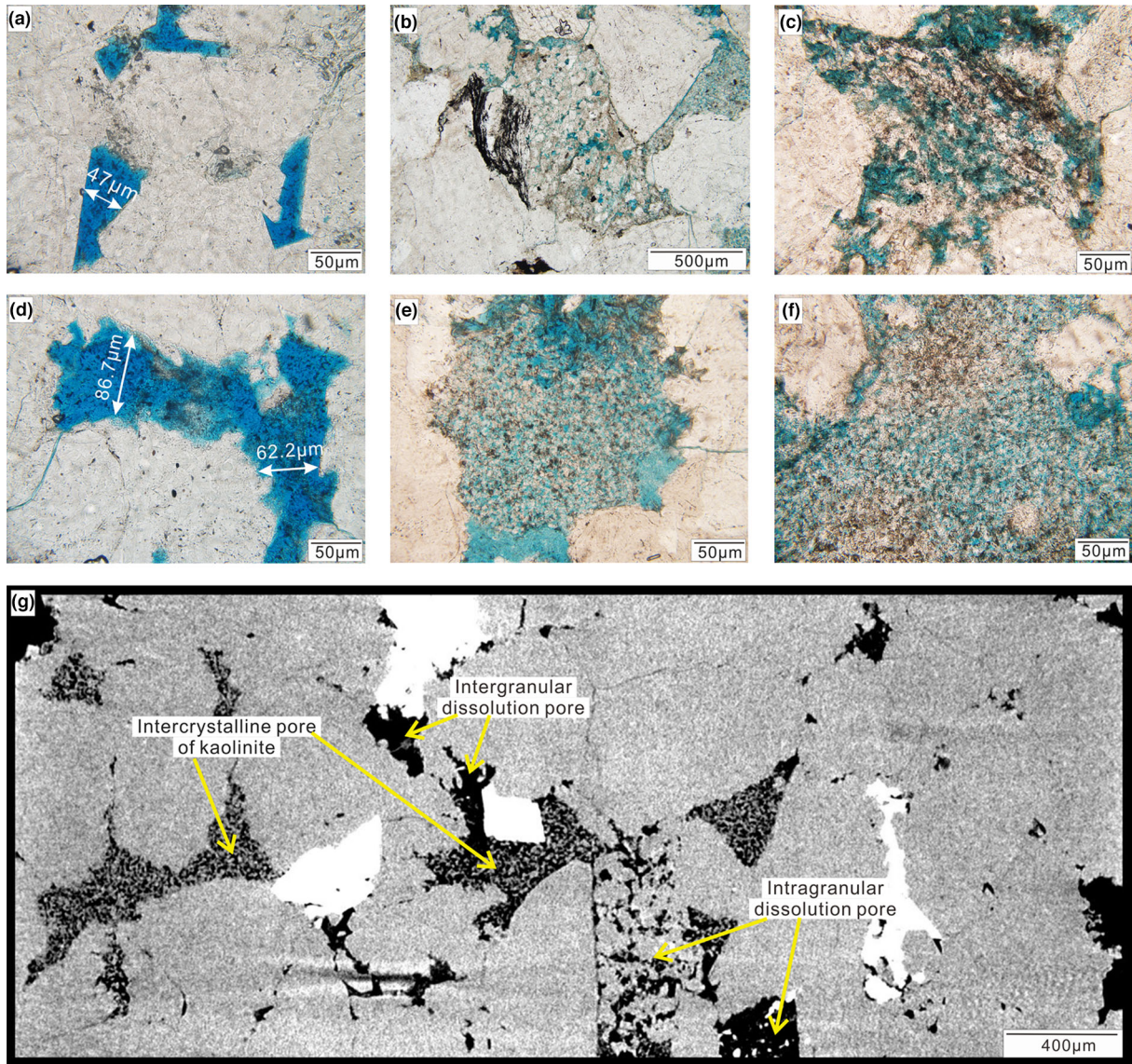


Figure 4. Typical thin section and CT images of different pore types in the study area. (a) Residual inter-granular pores with triangular or polygon pore shapes, Well L18, 4,339.0 m, PPL; (b) The honeycomb lithic dissolution pores, Well L12, 3,547.9 m, PPL; (c) The honeycomb lithic dissolution pores, Well L12, 3,547.0 m, PPL; (d) Inter-granular dissolution pores with obvious dissolved grain edge, Well L18, 4,339.0 m, PPL; (e) Kaolinite inter-crystalline pores, Well E33, 3,800.44 m, PPL; (f) Kaolinite inter-crystalline pores, Well L12, 3,547.9 m, PPL; (g) 2D-CT gray scale images of different types of pores, Well Y4, 3,541.3 m, CT. (PPL = plane polarized light).

under SEM (Fig. 5g, h). As temperature increased, the shape and heterogeneity of inter-crystalline pores changed simultaneously with kaolinite structural order and crystal size. At great depth, illite grows at the expense of blocky dickite crystals and is found intercalated within vermicular stacks of kaolinite (Lanson et al., 2002). Because the depth of all the samples obtained generally exceeded 3500 m, this would explain the complex inter-granular pore.

Overall, it can be seen that the samples from the study area had diverse pore shapes and a complex-connected pore network.

Pore-Throat Size Distribution

The HPMI results showed that the displacement pressures (p_d) of all samples fell between 0.04

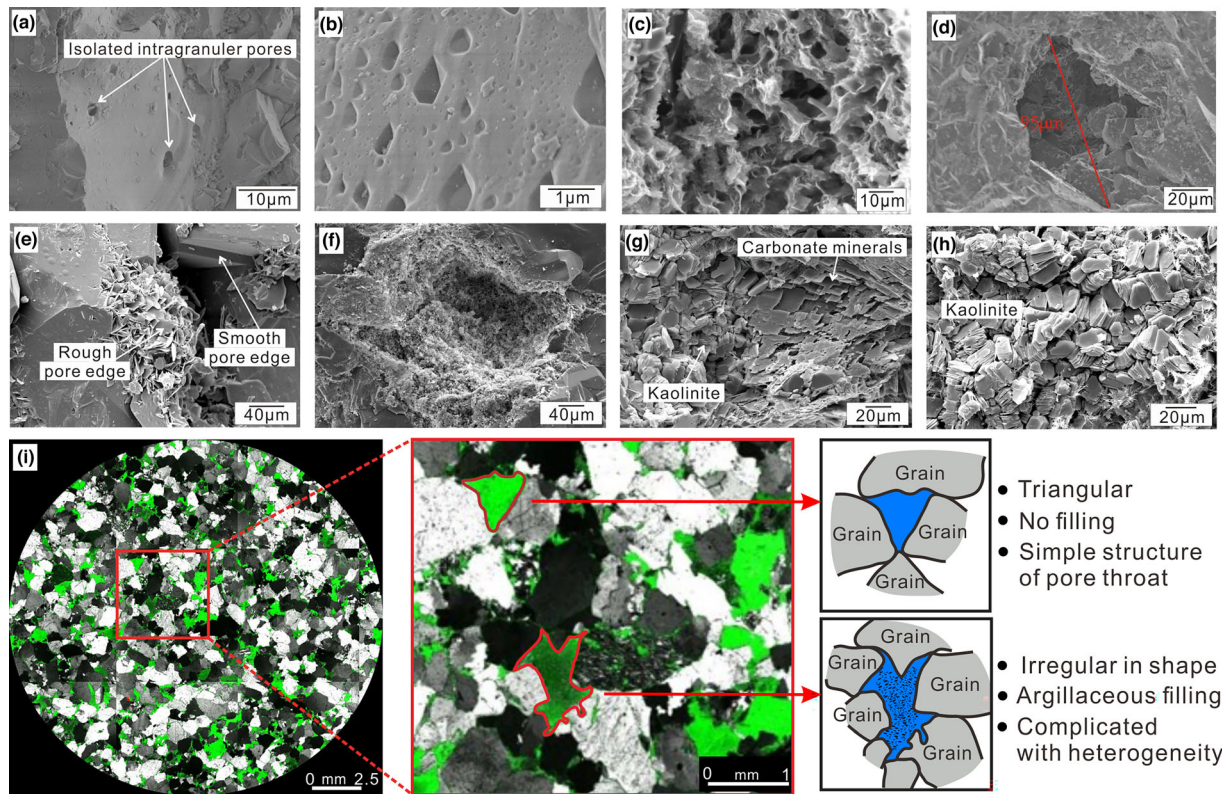


Figure 5. Typical SEM and laser confocal images were selected to illustrate the complexity of pore-throat structure of tight sandstone in He 8 and Shan 1 Members. (a) Intra-granular dissolution pores with clear and smooth pore edges, Well L7, 4,045.6 m, SEM; (b) Intra-granular dissolution pores with clear and smooth pore edges, Well Y3, 3,667.0 m, SEM; (c) Some dissolved rock debris and feldspar exhibit poor connection of pores, Well L18, 4,341.3 m, SEM; (d) Residual inter-granular pores in the regular shape, Well Li3, 3,773.9 m, SEM; (e) Residual inter-granular pores partially covered or clogged with authigenic clay mineral, Well L4, 3,864.9 m, SEM; (f) Residual inter-granular pores completely covered or clogged with authigenic clay mineral, Well E32, 3,758.3 m, SEM; (g) Inter-crystalline pores developed between vermicular kaolinite, Well S308, 3,960.2 m, SEM; (h) Inter-crystalline pores developed between needle flaky illite and vermicular kaolinite, L16, 3,611.8 m, Well SEM; (i) The pore-throat complexity does vary in the same pore types, Well S6, 3,314.3 m, laser confocal.

and 1.50 MPa, with mean of 0.56 MPa, with corresponding maximum pore radii (R_{max}) between 0.39 and 20.98 μm . The saturation median pressures (p_m) of all samples had a very wide distribution range, from 0.26 to 58.13 MPa, with mean of 9.76 MPa. The average pore-throat radii (R_a) ranged from 0.13 μm to 9.66 μm , with average of 1.51 μm . This revealed characteristics of low concentration and poor homogeneity of pore-throat size distribution.

The HPMI curve can be used to calculate the distribution relationship of pore-throat. Based on the classifications of Xoaoth (1966) and Li et al. (2017), reservoir space can be divided into four categories: macropores (> 1000 nm), mesopores I (250–1000 nm), mesopores II (100–250 nm) and transitional pores and micropores (< 100 nm). According to the HPMI curve, HPMI parameters,

pore-throat distribution characteristics and physical properties, all samples were divided into the following three types.

Type A: The storage capacity, seepage capacity and pore-throat distribution were the most conducive reservoirs among all types. Porosity ϕ was between 10.1 and 12.8%, with mean of 11.4%. The permeability ranged from 1.01 to 25.30 mD, with average of 9.08 mD. Storage space consisted mainly of macropores, and the pore-throat volumes with macropores, mesopores I, mesopores II and transitional pores and micropores accounted for 55.36, 27.96, 6.18 and 10.50%, respectively, of the total pore volume. The HPMI curves of Type A samples are presented in Figure 6. The curve has a wider horizontal stage at the early stage of mercury injection. These samples had maximum R_{max} , R_a and

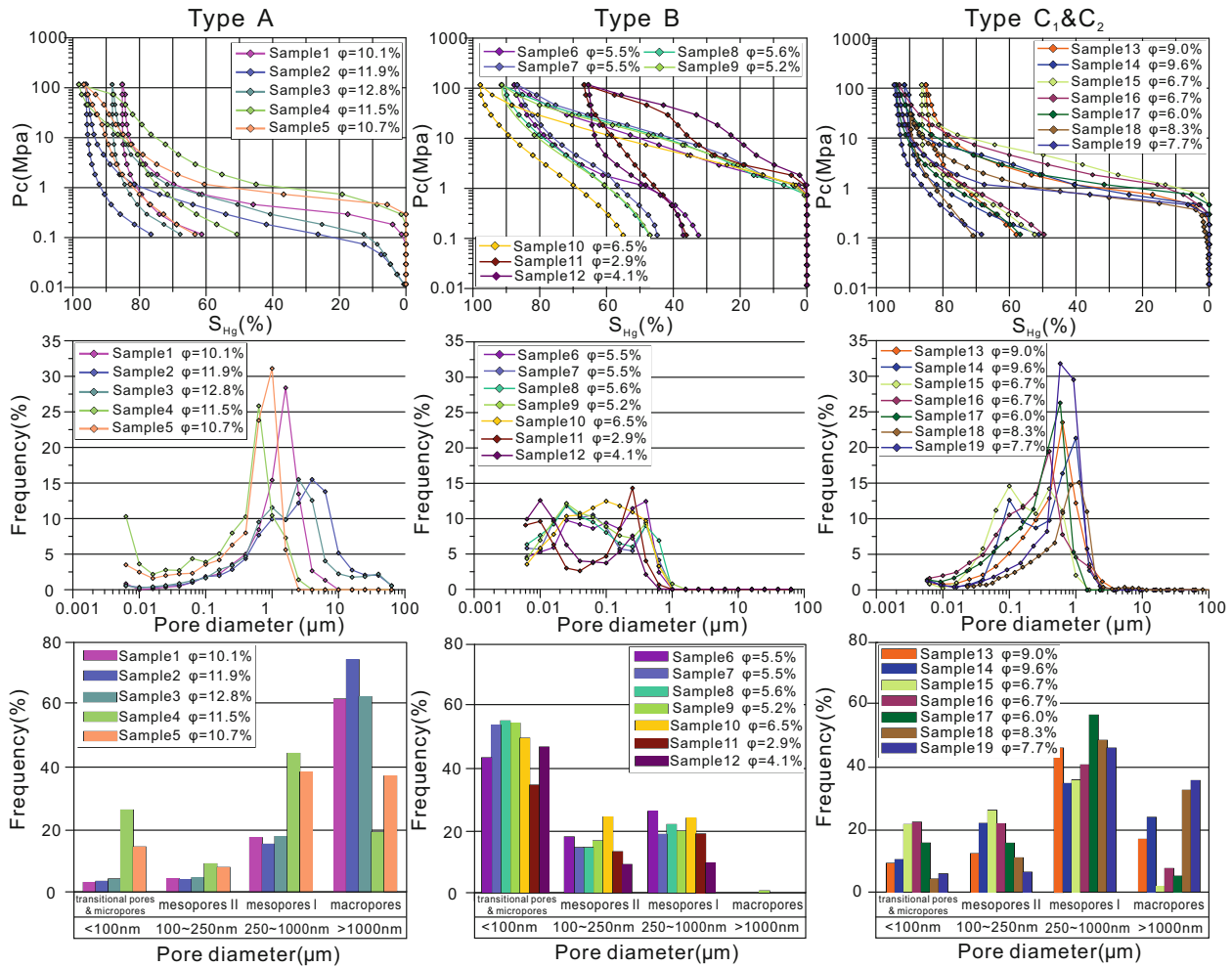


Figure 6. Mercury saturation curves, pore size distribution curves and pore size histograms of Type A, B and C samples obtained from HPMI test.

R_m (median pore-throat radiuses), corresponding to minimum p_d and p_m .

Type B: The physical properties and pore-throat distribution were the worst among all types. Porosity was between 2.9 and 6.5%, with average of 5.04%. Permeability ranged from 0.08 mD to 0.18 mD, with average of 0.13 mD. The pore sizes of all samples had a narrow range, from 3.6 to 1000 nm, and the peak being concentrated between 10 and 400 nm. These samples had almost no macropores, and the pore-throat volumes with mesopore I, mesopores II and transitional pores and micropores accounted for 23.73, 18.54 and 53.73%, respectively, of the total pore volume. The slope of the mercury intrusion curve was very steep at the initial stage of mercury injection (Fig. 6). Increasing mercury

intrusion pressure resulted in the curve displaying a narrow end stage. These samples had minimum R_{max} , R_a and R_m , and were predominantly dry formation.

Type C: This type was characterized by medium physical property and pore-throat parameters of between Types A and B. The porosity of Type C was between 6.0 and 9.6%, and the permeability ranged from 0.32 to 1.31 mD (Fig. 6). Mesopores were the main reservoir spaces in Type C.

Fractal Characteristics

The values of D of all samples displayed three- or four-stage forms (Fig. 7). The D_1 , D_2 , D_3 and D_4

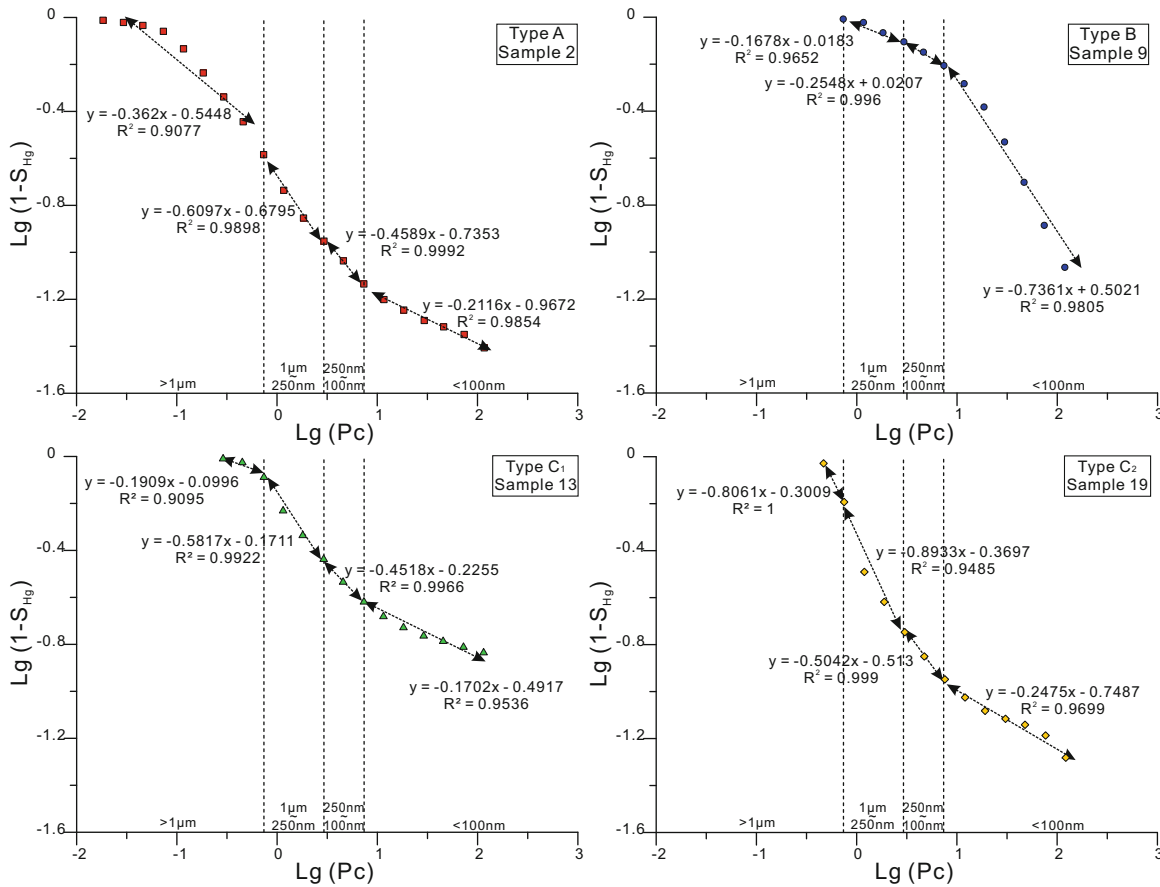


Figure 7. The $\log(1-S_{Hg})$ versus $\log(p_c)$ plot of Type A, B, C₁ and C₂ samples using capillary pressure wet-phase saturation method.

are the fractal dimensions of macropores, mesopores I, mesopores II and transitional pores and micropores, respectively (some samples lacked D_1) (Xoath, 1966; Li et al., 2017). Overall, the correlation coefficient R^2 was larger than 0.9 and the mean value was 0.977, showing high correlation.

The D data of all samples are shown in Table 3. The values of D of Type A samples can be divided into four stages. The D_{total} ranged between 2.2998 and 2.7179, with mean of 2.5245. Due to the absence of macropores in Type B samples, the values of D exhibited three-segment change patterns. The results showed that the averages of D_2 and D_3 were 2.7841 and 2.7527, respectively, and D_4 , with the largest proportion of pore volume, varied between 2.0577 and 2.7214, with average of 2.4109, suggesting good degree of homogenization of transitional pores and micropores. The values of D of Type C samples displayed three- or four-segment changes. Accord-

ing to D_{total} differences, the samples could be divided further into two categories: Types C₁ ($D_{total} > 2.45$) and C₂ ($D_{total} < 2.45$). D_{total} for Type C₁ ranged from 2.4623 to 2.5609, with average of 2.5256, while D_{total} for Type C₂ ranged between 2.2081 and 2.4079, with mean of 2.3307. This demonstrates that, although the pore-throat radius distributions of the two types were similar, the degree of microscopic pore-throat heterogeneity of Type C₁ was much greater than that of Type C₂.

According to the weighted mean of porosity of macropores, mesopores I, mesopores II and transitional pores and micropores, the piecewise and total fractal dimension of different scale pores could be obtained. The D_{total} ranged between 2.2081 and 2.7510, with mean of 2.5053. The pore-throat structure of tight sandstones from the Tianhuan Depression was complex, and the microscopic heterogeneity varied greatly.

Table 3. Results of porosity and piecewise D for different pore size ranges. Note: D_1 = piecewise D of macropores; ϕ_1 = porosity of macropores; D_2 = piecewise D of mesopores I; ϕ_2 = porosity of mesopores I; D_3 = piecewise D of mesopores II; ϕ_3 = porosity of mesopores II; D_4 = piecewise D of transitional pores and micropores; ϕ_4 = porosity of transitional pores and micropores; D_{total} = total D

Type	Sample	D_1	R^2	ϕ_1	D_2	R^2	ϕ_2	D_3	R^2	ϕ_3	D_4	R^2	ϕ_4	D_{total}
A	1	2.3182	0.9685	7.26	2.5845	0.987	2.02	2.7768	0.9977	0.48	2.9471	0.8971	0.34	2.4142
	2	2.6380	0.9077	9.16	2.3903	0.9898	1.84	2.5411	0.9992	0.48	2.7884	0.9854	0.42	2.6011
	3	2.7517	0.8475	9.02	2.5540	0.9769	2.56	2.7299	0.9827	0.64	2.9010	0.9556	0.58	2.7179
	4	2.7833	0.9871	2.24	2.4430	0.9689	5.16	2.6950	0.9975	1.05	2.6594	0.9852	3.04	2.5896
	5	2.0646	0.9972	4.07	2.3520	0.9597	4.22	2.5992	0.9999	0.86	2.6070	0.9807	1.56	2.2998
B	6	–	–	–	2.6958	1	1.65	2.6950	0.9973	1.13	2.4492	0.994	2.72	2.5736
	7	–	–	–	2.8227	0.9832	1.18	2.7847	0.9822	0.92	2.4074	0.9883	3.40	2.5599
	8	–	–	–	2.8093	0.9901	1.34	2.7748	0.9942	0.89	2.2808	0.9655	3.37	2.4862
	9	–	–	–	2.8322	0.9652	1.18	2.7452	0.996	0.94	2.2639	0.9805	3.08	2.4795
	10	–	–	–	2.7400	0.9966	1.59	2.5801	0.9969	1.61	2.0577	0.966	3.30	2.3544
	11	–	–	–	2.6995	0.9916	0.83	2.8053	0.9747	0.58	2.7214	0.9018	1.50	2.7318
	12	–	–	–	2.8892	0.9042	0.61	2.884	0.9891	0.57	2.6960	0.9082	2.92	2.7510
C														
C ₁	13	2.8091	0.9095	1.79	2.4183	0.9922	4.89	2.5482	0.9966	1.32	2.8298	0.9536	1.00	2.5609
	14	2.4736	1	2.52	2.5623	0.9954	3.65	2.1520	0.9726	2.33	2.7600	0.8496	1.10	2.4623
	15	–	–	–	2.6635	0.9942	2.95	2.3934	0.9851	2.05	2.5402	0.9003	1.70	2.5497
	16	2.8969	1	0.56	2.5645	0.9654	2.93	2.3882	0.9985	1.59	2.4785	0.9953	1.62	2.5295
C ₂	17	–	–	–	2.3294	0.9968	3.97	2.4031	0.9999	1.01	2.5308	0.9902	1.02	2.3761
	18	2.44	0.98	2.78	2.33	0.99	4.13	2.51	0.99	0.90	2.69	0.99	0.49	2.41
	19	2.1939	1	2.92	2.1067	0.9485	3.75	2.4958	0.999	0.54	2.7525	0.9699	0.49	2.2081

DISCUSSION

Relationship Between Mineral Compositions and Reservoir Properties

Figure 8 shows scatter plots of the main mineral components of tight sandstones with their porosity and permeability. Compared with most ductile rock debris, quartzite debris was more similar to quartz in chemical composition and compaction resistance. Therefore, quartzite debris was excluded from the rock debris content and converted to quartz content. Rigid minerals, which can stabilize the rock framework and protect primary pores from destruction caused by mechanical compaction (Dong et al., 2017), have stronger compaction resistance compared to ductile minerals. Conversely, among rigid grains, ductile minerals are deformed easily because of intensive compaction, which greatly reduces a reservoir's seepage capacity (Li et al., 2019). Therefore, as shown in Figure 8, quartz and quartzite debris contents were correlated positively with permeability and porosity, with correlation coefficients of R^2 of 0.3709 and 0.438, respectively. However, with increase in content of rock debris (except quartzite debris), the decreasing trend in permeability and porosity was not significant shown by the

correlation coefficients R^2 of 0.3903 and 0.2878. The contents of rigid grains (quartz and quartzite debris) ranged from 59.5 to 99.4%, with average of 81.5%, which was much higher than that of ductile minerals content. Therefore, the preservation effect of rigid grains on porosity and permeability must be stronger than the destructive effects of ductile minerals, resulting in a correlation between the content of rigid grains and physical properties being slightly better than that of ductile minerals. Clay mineral content of all samples was lower than 16%, and the correlation between clay mineral content and reservoir physical properties yielded no distinct reservoir controlling trends (Fig. 8).

Relationship Between Physical Properties and Fractal Characteristics

Measuring physical properties by fractal analysis is an effective method (Bu et al., 2015). Firstly, the correlation between D_{total} and physical properties was analyzed according to sample classification (Fig. 9). Previous research has generally supposed that fractal dimension has negative correlation with porosity and permeability in tight sandstone (Sun et al., 2019; Wu et al., 2019). However, there was no

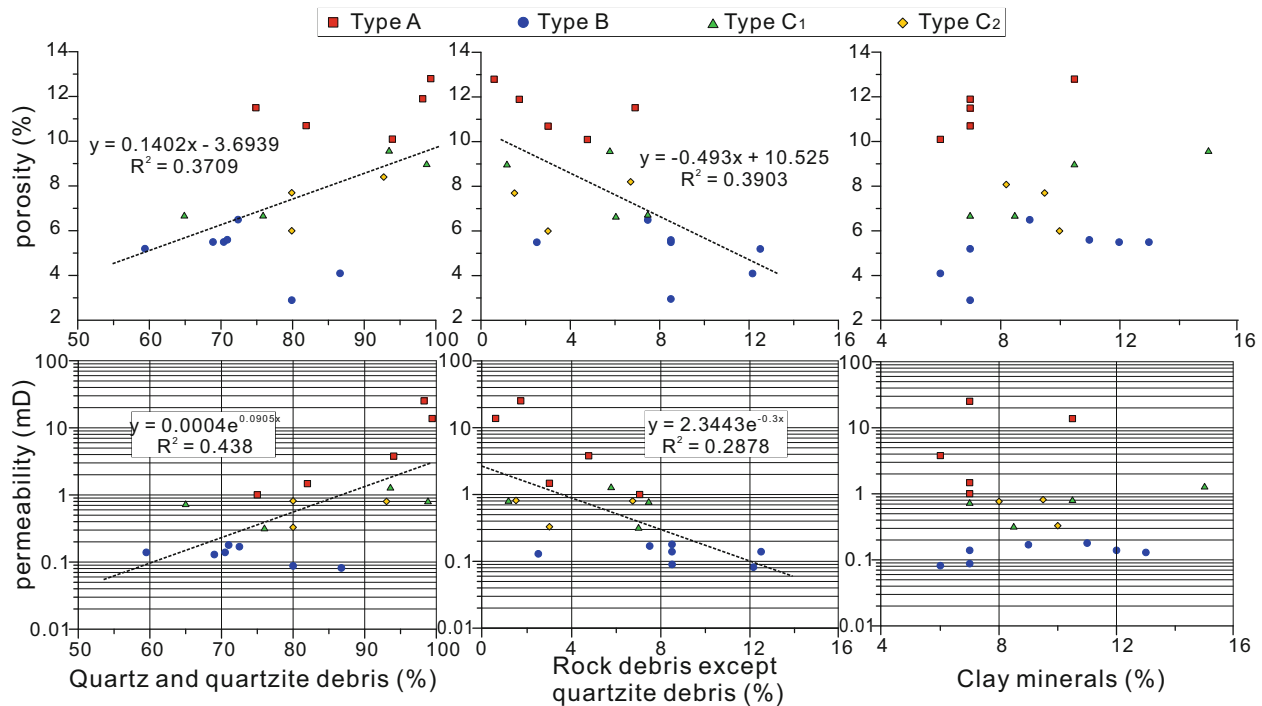


Figure 8. Scatter diagram of different types of mineral content and petrophysical properties.

significant correlation between the D_{total} and physical properties for all samples in this study (Fig. 9). If Type A data were eliminated, however, a negative correlation could be observed. As mentioned above, Type A samples were mixed with large amounts of macropores beyond 1000 nm. The proportion of bound water to different-size pores was very different, which led to a great difference in their ability to modify pore morphology (Sun et al., 2019). The irregularity of pore morphology distribution at different scales changed the specific surface and complexity of pore distribution (Corrado et al., 2014; Wu et al., 2019). By contrast, the pore-throat radius of Types B and C samples was concentrated mainly below 1000 nm (micropores, transitional pores and mesopores), which seemed to indicate that the negative correlation was more applicable to pores below 1000 nm.

Subsequently, the piecewise D and porosity of the differing ranges of pore size was analyzed by linear regression (Fig. 10) to understand more precisely the relationship of storage capacity with pore-throat characteristics. The results showed that piecewise D (i.e., D_2 , D_3 and D_4) and their corresponding porosity (ϕ_2 , ϕ_3 and ϕ_4) presented clear exponential negative correlation, while there

seemed to be no correlation between D_1 and ϕ_1 . This indicates that lower values of D (poor microscopic pore structure heterogeneity) are often accompanied by better reservoir capacity. However, this effect was most pronounced when the pore-throat radius was less than 1000 nm. This confirms that fractal analysis could be adopted as one of the indicators to evaluate comprehensively the reservoir physical properties only for pores with sizes of less than mesopore (i.e., < 1000 nm). If the pore-throat radius reaches a macropore level, this relationship seems to become ambiguous.

Pore connectivity is also an important indicator of the degree of microscopic pore-throat heterogeneity (Qiao et al., 2019). The results obtained from micro-CT provided further evidence of good correspondence between complexity of pore-throat structure and storage capacity. Table 4 shows micro-CT scanning and the corresponding parameters of three tight sandstone samples. The CT porosity of sample S_1 was as high as 9.88%. The two-dimensional CT images showed that the pores were generally well developed, and composed mainly of inter-granular pores and loosely accumulated kaolinite inter-crystalline pores (Fig. 5i). In the three-dimensional CT images (Table 4), the whole

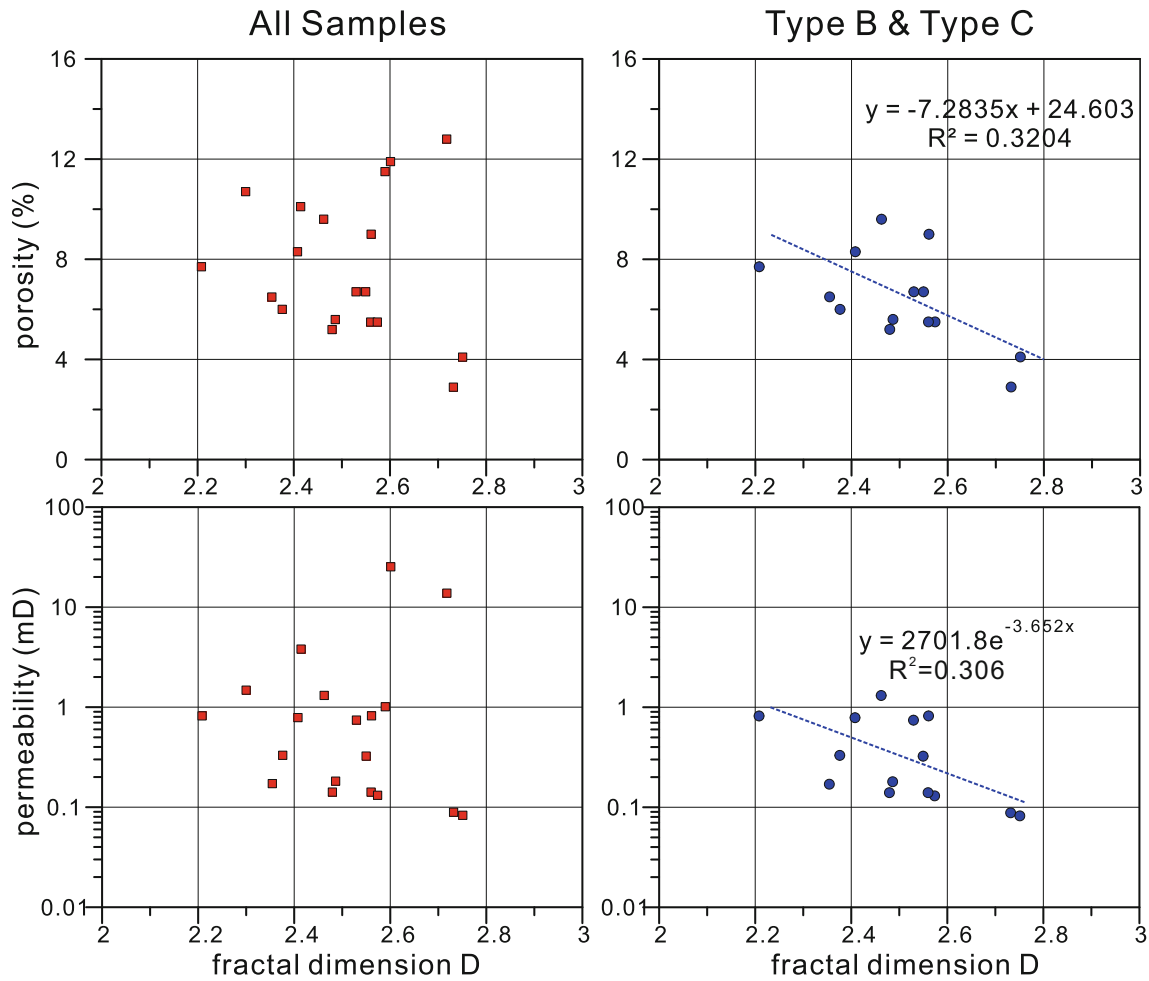


Figure 9. The relationship between the total fractal dimension and physical properties in different types of samples.

pore network showed quite high homogeneity and comparatively regular pore-throat morphology. Only a small number of pores were separated from the main pore network, and the pore-throat connectivity was as high as 74.27%. In contrast, the CT porosity of sample S_2 decreased to 7.7%, and a significant reduction in the radius of the pore-throat can be observed through a CT image. Correspondingly, the morphological characteristics of rugged pore edges were more distinct. In three-dimensional images, the isolated distribution of irregular pores was more frequent, and the pore-throat connectivity was poor. As sample S_3 had the lowest CT porosity, and its pore type was composed mainly of extremely compact kaolinite inter-crystalline pores. The pore size varied greatly in the three-dimensional images. Irregular pores were mostly distributed in isolation

and the pore-throat connectivity was only 28.64%. These results further confirm that tight sandstone with good reservoir capacity usually corresponds to a large pore-throat radius, regular pore-throat shape and homogeneous pore-throat network. However, as the porosity decreased, it is usually accompanied by transformation of pore type, rapid decrease of pore connectivity and significantly enhanced microscopic pore-throat heterogeneity.

Controls of HPMI Parameters on Fractal Characteristics and Physical Properties

Fitting relationship curves were made between piecewise D and HPMI parameters such as R_{max} , p_d , R_m , p_m , R_a and S (skewness) to characterize the

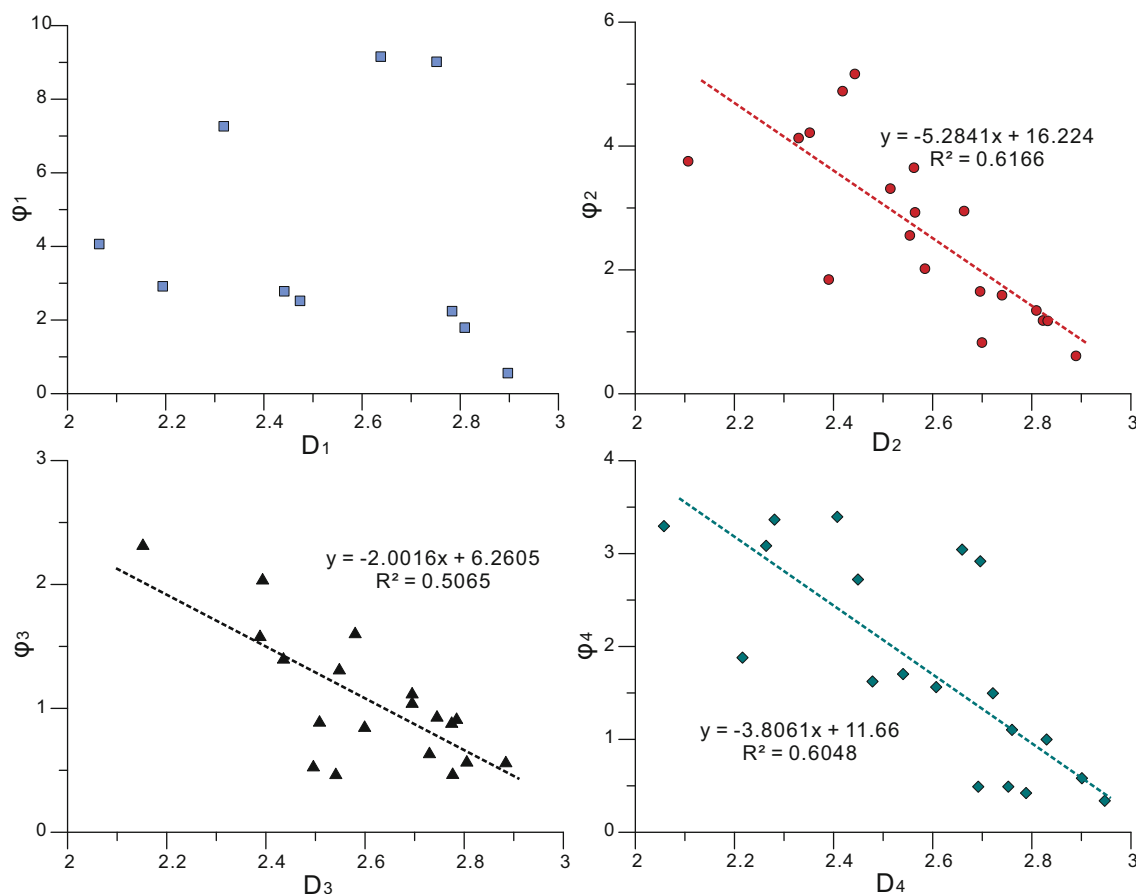


Figure 10. The relationship between the piecewise fractal dimension and corresponding porosity.

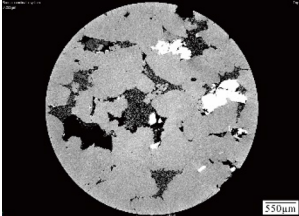
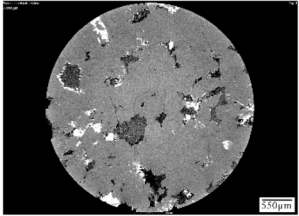
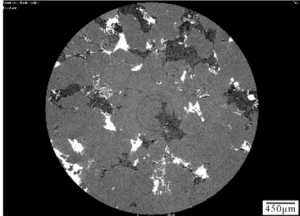
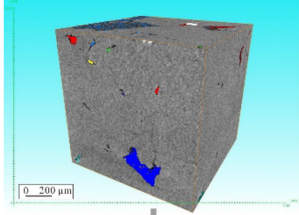
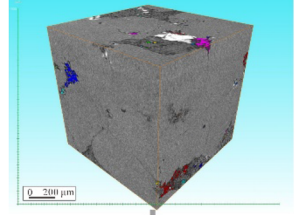
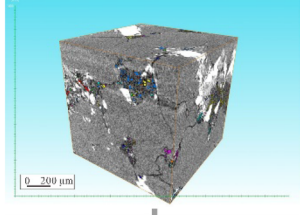
relationships between HPMI parameters and fractal properties. The correlation characteristics and testing parameters are shown in Table 5 and Figure 11. Although there is no relation between D_{total} and HPMI parameters, the piecewise D had a certain correlation with HPMI parameters. D_2 had the best correlation with HPMI parameters, being correlated positively with p_m ($R^2 = 0.6075$) and correlated negatively with R_m ($R^2 = 0.5897$). Although the correlation between D_4 and HPMI parameters was also relatively strong (Fig. 11), D_2 had good positive correlations with p_m , p_d and negative correlations with R_{max} , R_m , R_a , while D_4 had the exact opposite correlations with these parameters. These indicate that the controlling factors of pore structure on heterogeneity varied in different pore ranges. In addition, as for D_1 and D_3 , with the exception of the

correlation between D_1 and S , there was no obvious correlation with other HPMI parameters.

In summary, D_2 had the greatest influence on HPMI parameters, and the heterogeneity, pore surface roughness and anisotropy of Mesopore I were the main factors that controlled the pore-throat structure in He 8 and Shan 1 Members. However, the lack of correlation between D_{total} and HPMI parameters was caused by the superposition effect of different correlations (positive or negative) between the piecewise D and the HPMI parameters (Wu et al., 2019). Therefore, the relationship among fractal properties, porosity and HPMI parameters showed that D can be used as one of the indicators in a comprehensive evaluation of pore-throat structure characteristics.

In addition to values of D , the correlations between the HPMI parameters and reservoir proper-

Table 4. 2D and 3D pore network visualization model and related parameters based on CT technology for the samples in He 8 and Shan 1 Members in the study area

Sample	S ₁	S ₂	S ₃
Well name	Y4	S315	Z3
Member	He 8	He 8	He 8
Depth	3541.03m	3750.63m	3541.03m
CT porosity	9.88%	7.7%	6.7%
Connectivity rate	74.27%	47.89%	28.64%
2D images			
3D images			
Microscopic heterogeneity	Low	Middle	High

ties (total porosity and permeability) were analyzed and compared in Figure 12 and Table 5. R_{max} was correlated positively with total porosity and permeability, and the correlation coefficients R^2 are 0.6784 and 0.8546, respectively. Similarly, with increase in R_m and R_a , the total physical properties also showed an increasing trend, and the correlation coefficient R^2 was above 0.75. These results imply that with increasing proportion of macropores, the reservoir

and seepage capacity of tight sandstone will improve. However, the correlation between HPMI parameters and porosity at different scales was different. Overall, the correlation between various HPMI parameters (except the skewness) and ϕ_1 was the best, followed by ϕ_4 . As for ϕ_2 , p_m and R_m had certain correlations with ϕ_2 , and the correlation coefficients were 0.4065 and 0.4079, respectively. Beyond this, no significant correlation was found.

Table 5. Correlation coefficients among D , physical properties and HPMP parameters. Note: D_1 = piecewise D of macropores; D_2 = piecewise D of mesopores I; D_3 = piecewise D of mesopores II; D_4 = piecewise D of transitional pores and micropores; ϕ_{total} = total porosity; ϕ_1 = porosity of macropores; ϕ_2 = porosity of mesopores I; ϕ_3 = porosity of mesopores II; ϕ_4 = porosity of transitional pores and micropores

Parameters	Displacement pressure (P_d)	Maximum pore radius (R_{max})	Median pressure (P_m)	Median pore radius (R_m)	Average pore throat radius (R_a)	Skewness (S)
Fractal dimensions						
D_1	0.0226	0.0234	0.0731	0.069	0.0138	0.4479
D_2	0.2782	0.2912	0.6075	0.5897	0.3246	0.3788
D_3	0.0111	0.02	0.1899	0.1959	0.0357	0.0768
D_4	0.2219	0.1954	0.288	0.2578	0.4112	0.3809
D_{total}	0.0001	0.0023	0.1481	0.1609	0.0001	0.1744
Physical properties						
Permeability	0.8254	0.8546	0.8188	0.8062	0.9062	0.0165
ϕ_{total}	0.6424	0.6784	0.7979	0.7939	0.7560	0.0256
ϕ_1	0.6434	0.6528	0.8725	0.8724	0.8781	0.0227
ϕ_2	0.0693	0.0883	0.4065	0.4079	0.1162	0.1726
ϕ_3	0.1087	0.0836	0.0059	0.0032	0.0776	0.0223
ϕ_4	0.3174	0.3065	0.5394	0.5067	0.5331	0.4860

These results imply that the control effect of HPMP parameters on physical properties was reflected mainly in the macropores, transitional pores and micropores, which was different from that of piecewise D .

Comprehensive Reservoir Factors on the Prediction of Gas-Bearing Capacity

The microscopic pore-throat structure parameters and macroscopic petrophysical properties of different reservoir types are provided in Table 6. Integrated analysis implies that the storage space of Type A samples consisted mainly of micrometer-scale inter-granular pores as well as honeycomb intra-granular dissolution pores. Type A was the best among the four types in terms of pore-throat structure and physical properties and the logging interpretation results were generally gas formations. In contrast, Type B samples had low porosity and permeability. Moreover, the reservoir space was composed primarily of transitional pores and micropores less than 100 nm. Gas migration and accumulation need to overcome great capillary pressure, which makes it difficult to become favorable reservoirs in light of insufficient hydrocarbon generation power and the long-term migration of source rocks. Therefore, the logging interpretation results were generally dry formations. The physical

properties of Types C_1 and C_2 samples ranged between the former two types, and reservoir space was dominated by mesopores. However, there was a clear difference in the interpretation of the results. Most of the Type C_1 samples were gas formations, while most of the Type C_2 samples were poor-gas formations, indicating that the gas-bearing capacity cannot only be interpreted by physical properties and HPMP parameters. The characteristics of physical properties and values of D_{total} of different types of samples are demonstrated in Figure 13. Type C_1 samples had larger D_{total} , signifying that pore-throat heterogeneity was higher. The D_{total} of Type C_2 samples were less than 2.45, indicating that pore-throat structure was more uniform than in Type C_1 samples. Previous studies generally highlight that poor microscopic pore-throat heterogeneity is not favorable for oil and gas storage, which seems to contradict the results of this study.

Combining the pore-throat distribution characteristics with the thin section and SEM, the inter-crystalline pores of clay minerals and dissolution pores at a nanometer scale formed the main gas reservoir spaces in these two types of samples. The difference in pore-throat heterogeneity may be related to the degree of recrystallization, transformation and the diversity of growth forms of authigenic clay minerals. The two groups of clay minerals most often encountered in the study area were kaolinite and illite. Microscopic observation showed that illite

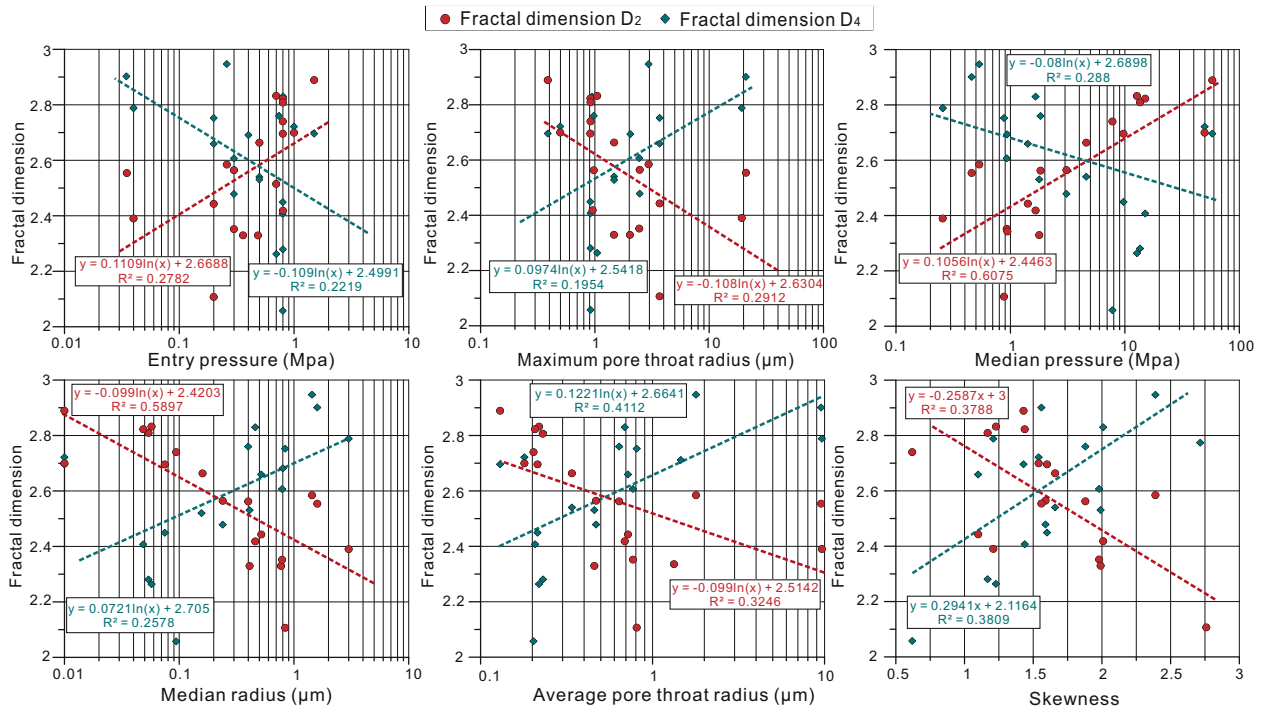


Figure 11. The relationship between the piecewise fractal dimension and HPMI parameters.

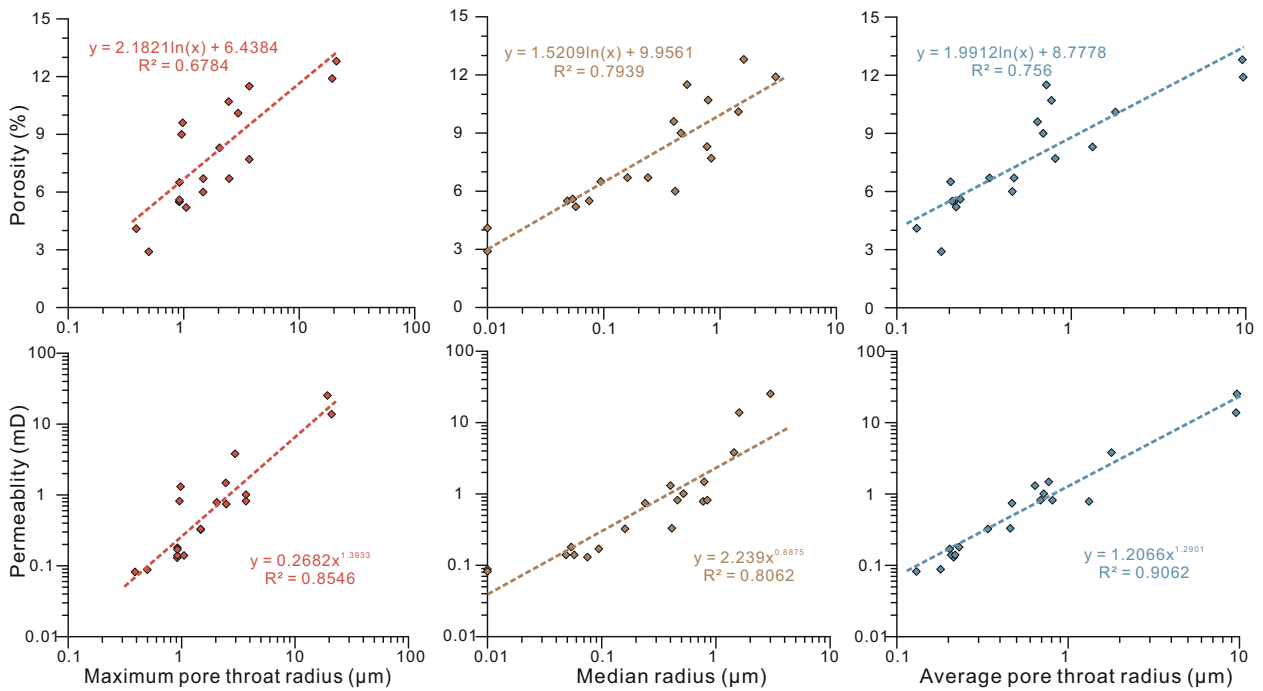


Figure 12. The relationship between physical properties and HPMI parameters.

Table 6. Summary of four types of tight reservoirs in gas-bearing capacity based on HPMI parameters, reservoir physical properties, pore-throat characteristics and other aspects

Type	HPMI Parameters				Macroscopic physical characteristics				Pore-throat distribution				Schematic diagram of main reservoir space			Pore-throat characteristics		Gas-bearing capacity	
	Displacement pressure (MPa)	Maximum pore radius (μm)	Median pore radius (μm)	Average pore-throat radius (μm)	Skewness	Properties	Porosity (%)	Permeability (mD)	Sample 12	Sample 12	Sample 12	Sample 12	Brittle mineral	Pore	Clay mineral	Formation	Main controlling factor		
Type A	0.04-0.30 0.17	2.45-20.98 9.88	0.26-1.42 0.72	0.52-3.00 1.47	0.72-2.66 4.50	High	10.10-12.80 11.40	1.01-25.30 9.08	Sample 2	Sample 2	Sample 2	Sample 2				Dominated by intergranular dissolved pores, residual intergranular pores and intergranular dissolution pores, and the pore size is more than 1000 nm.	Dominated by gas-bearing formation	Physical properties & Pore type	
Type B	0.70-1.50 0.91	0.39-1.05 0.80	7.79-58.13 23.85	0.01-0.09 0.05	0.13-0.23 0.20	Low	2.90-6.50 5.04	0.08-0.18 0.13	Sample 12	Sample 12	Sample 12	Sample 12				Pore size is less than 100 nm, and the reservoir is extremely tight.	Dominated by dry formation	Physical properties & Pore type	
Type C₁	0.30-0.80 0.59	0.96-2.47 1.47	1.66-3.61 2.80	0.16-0.46 0.32	0.34-0.69 0.54	Medium	6.70-9.60 8.00	0.32-1.31 0.80	Sample 12	Sample 12	Sample 12	Sample 12				Dominated by kaolinite intercrystalline pores with pore size ranging from 100 nm to 1000 nm, showing microscopic pore-throat heterogeneity	Gas-bearing formation	Microscopic pore-throat heterogeneity	
Type C₂	0.20-0.50 0.35	1.47-3.70 2.40	0.88-1.79 1.21	0.41-0.84 0.67	0.46-1.32 0.86	Medium	6.00-8.30 7.33	0.33-0.82 0.64	Sample 12	Sample 12	Sample 12	Sample 12				Dominated by kaolinite intercrystalline pores with pore size ranging from 100 nm to 1000 nm, showing weak microscopic pore-throat heterogeneity	Poor gas-bearing formation	Microscopic pore-throat heterogeneity	

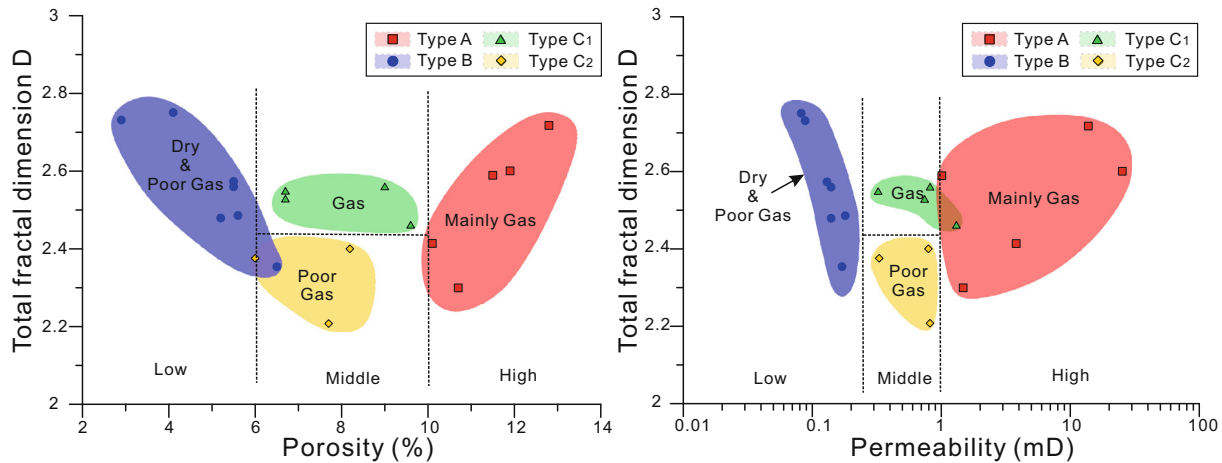


Figure 13. The relationship between the total fractal dimension and physical properties. The red areas represent Type A samples, which are dominated by gas formations. The blue areas represent Type B samples, which are dominated by dry and poor gas formations. The green areas represent Type C₁ samples, which are dominated by gas formations. The yellow areas represent Type C₂ samples, which are dominated by poor gas formations.

was mainly derived from illitization of kaolinite rather than the continuous reaction via mixed-layer illite–smectite. Compared with Type C₂, the kaolinite in Type C₁ samples from gas formations tended to accompany illitization (Fig. 14). The formation of kaolinite was restricted to low temperature, shallow burial depths and before hydrocarbon charging, which was related to meteoric fluids or organic acid-rich fluids (Ehrenberg, 1991; De Ros, 1998; Lanson et al., 2002). The crystallization of illite at the expense of kaolinite often requires high temperature and high pressure conditions (Lanson et al., 2002; Martín-Martín et al., 2005; Mantovani et al., 2010) and usually occurs at the later stage of hydrocarbon generation. In fact, illitization of kaolinite has little effect on reservoir porosity. However, elongated, filamentous and lath-shaped illite can greatly enhance the microscopic pore-throat heterogeneity and capillary pressure. Because tight sandstone cannot solely be the preferred site for gas, it can also act as preservation for gas loss (Jiang et al., 2006). From the coupling relationship between hydrocarbon reservoir formation and diagenesis, we believe that the kaolinite inter-crystalline pores formed before hydrocarbon charging could provide good storage space. Illitization after hydrocarbon charging will increase pore-throat heterogeneity and capillary pressure, and prevent hydrocarbon losses. Thus, the significance of gas enrichment in Type C₁ is more likely to lie in good preservation conditions (Zhu et al., 2018), especially

in tight sandstone with kaolinite inter-crystalline pores as the main space.

In order to confirm further the relationship between microscopic pore-throat heterogeneity and gas-bearing capacity in Type C, we listed some actual well gas production rate data. Limited by actual data, we analyzed the relationship between the D of samples 15, 16, 18 and their average daily gas and water productions. For samples 15 and 16, the intervals where samples were located produced average gas yields of 41,000 m³/d and 57,000 m³/d, respectively, and no water was produced during the gas testing. Both two intervals were finally judged to be commercial gas reservoirs. In contrast, although in the interval where sample 18 was located produced an average gas yield of 26,900 m³/d, its water yield reached up to 28.5 m³/d. Such high water production severely limited the development of natural gas, which was ultimately judged to be a poor gas reservoir. It follows that when the physical properties and pore-throat type were nearly identical, the gas production capacity of the two types of samples differed greatly. Judging from the above-mentioned description, we deduced that microscopic pore heterogeneity played an important role. The difference in the values of D led to a great change of the preservation conditions. If the microscopic pore-throat heterogeneity of tight reservoir was too low, it is likely that its seal and preservation capacity of natural gas was insufficient after accumulation,

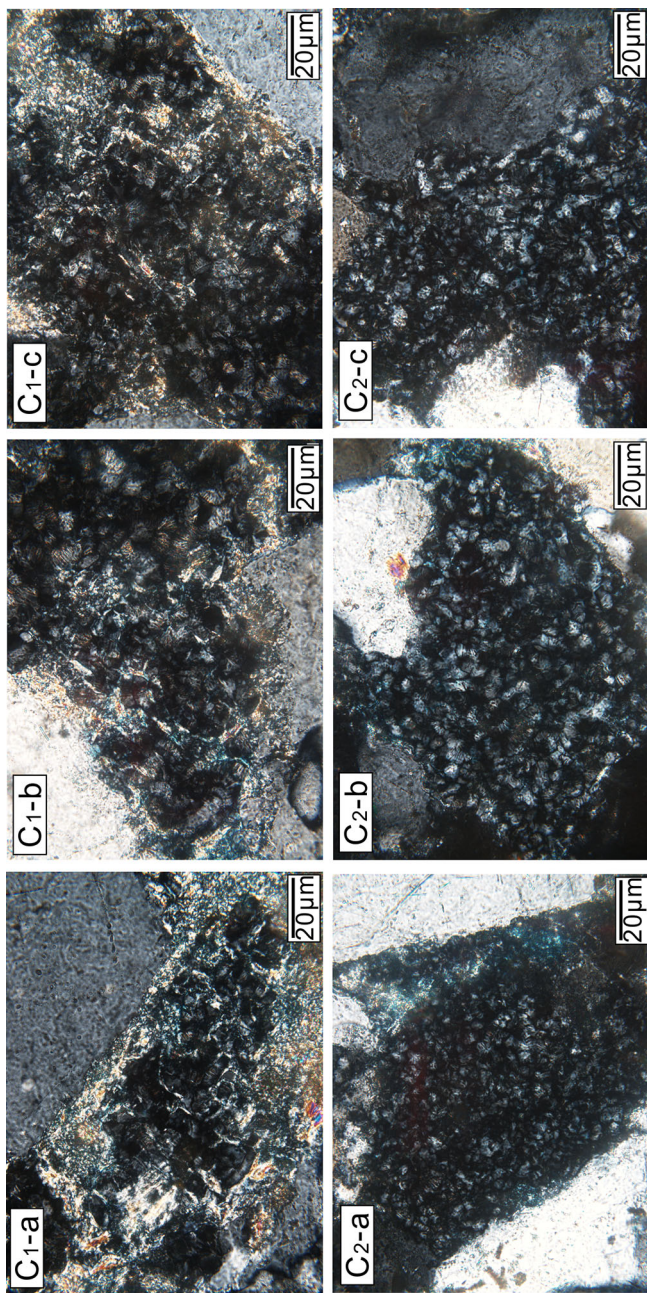


Figure 14. Comparison of the effect of illitization degree of kaolinite on inter-granular pores. (C1-a, b, c) Illitization with kaolinite makes pore-throat structure more complex, Sample 16, Well L13, 3,933.5 m, XPL. (C2-a, b, c) Kaolinite aggregates without illitization develops homogeneous inter-crystalline pores, Sample 19, Well L13, 3863.0 m, XPL. (XPL = cross-polarized light).

which ultimately led to the low gas content and high water content in the gas testing process.

Considering the above discussion, this study provides a novel idea for fractal analysis and the control of gas-bearing capacity in tight sandstone. First, the application of fractal theory seems to have certain limitations. For tight sandstones, it is only suitable for the reservoir space with smaller pore sizes. However, in conventional reservoirs with larger pore sizes, the importance of physical property conditions is increased greatly, and the applicability of fractal theory is inadequate. Secondly, the ideal tight sandstone has the characteristics of a combination of reservoir and preservation. In previous studies of fractal analysis, researchers limited their attention to the rock storage capacity, and ignored the dynamic relationship between gas preservation and rock tightness evolution. After tight sandstone accumulation, gas will still have secondary reformation, such as diffusion and migration. Therefore, rock diagenesis (dissolution, replacement, and recrystallization in the late diagenetic stage) after the peak of hydrocarbon generation is of great significance to gas preservation. If the microscopic pore heterogeneity increases in this stage, diffusion and migration of natural gas will be prevented, which is conducive to accumulation.

CONCLUSIONS

In this paper, the lithologic, physical, pore-throat, fractal and gas-bearing capacity of the tight sandstone of the He 8 and Shan 1 Members in the northern Tianhuan Depression of Ordos Basin was studied, and the following conclusions were drawn.

1. The primary reservoir storage of tight gas sandstone is within inter-granular dissolution pores and kaolinite inter-crystalline pores. The complexity and connectivity of different pore types are quite different. All the samples can be classified as Type A ($\phi > 10\%$, dominated by macropores), Type B ($\phi < 6\%$, dominated by transitional pores and micropores) and Type C ($6\% < \phi < 10\%$, dominated by mesopores) according to their physical properties and pore-throat radius distributions. Based on fractal dimension analysis, Type C can be divided further into Types C_1 ($D_{total} > 2.45$) and C_2 ($D_{total} < 2.45$).
2. Reservoir porosity and permeability significantly increase with increase in quartz content (including quartzite debris), while the increase of plastic debris content is unfavorable to reservoir physical properties. The piecewise D (D_2 , D_3 and D_4) and their corresponding porosity (ϕ_2 , ϕ_3 and ϕ_4) present a clear exponential negative correlation. There are certain correlations between piecewise D and various HPMI parameters although they respond well only at the mesopore and micropore level. This indicates that fractal analysis can be used as one of the indicators in the comprehensive evaluation of pore throat structure characteristics of tight sandstone only when the pore size is less than 1000 nm.
3. The physical properties and pore type are the major controlling factors of gas-bearing capability, leading to the difference of Type A as gas formation and Type B as dry formation. The microscopic pore-throat heterogeneity is a secondary factor. Illitization in late diagenesis increases the degree of microscopic pore-throat heterogeneity, thus providing good preservation conditions for gas accumulation. Therefore, Types C_1 and C_2 , which have similar physical properties and pore types, are gas formations and poor gas formations, respectively.
4. Finally, we drew the conclusion that the reservoir physical properties, pore types and microscopic pore-throat heterogeneity play joint roles in controlling the gas-bearing capacity.

ACKNOWLEDGMENTS

This work was supported by the National Natural Science Foundation of China (41872102; 41202107). We thank PetroChina Changqing Oilfield Company for permission to use industry data for this research. Thanks are also extended to the

reviewers for their valuable comments and constructive modifications that greatly enhanced the manuscript. We are grateful to chief Editor John Carranza and two anonymous reviewers for their valuable comments and suggestions, which contributed to the improvement of the article.

DECLARATIONS

CONFLICT OF INTEREST We declare that we do not have any conflict of interest in connection with the work submitted.

REFERENCES

- Broseta, D., Barré, L., Vizika, O., Shahidzadeh, N., Guilbaud, J. P., & Lyonnard, S. (2001). Capillary condensation in a fractal porous medium. *Physical Review Letters*, *86*(23), 5313–5316.
- Bu, H. L., Ju, Y. W., Tan, J. Q., Wang, G. C., & Li, X. S. (2015). Fractal characteristics of pores in non-marine shales from the Huainan Coalfield, Eastern China. *Journal of Natural Gas Science & Engineering*, *24*, 166–177.
- Cai, J. C., Yu, B. M., Zou, M. Q., & Mei, M. F. (2010). Fractal analysis of invasion depth of extraneous fluids in porous media. *Chemical Engineering Science*, *65*(18), 5178–5186.
- Corrado, S., Aldega, L., Celano, A. S., Benedetti, A. A. D., & Giordano, G. (2014). Cap rock efficiency and fluid circulation of natural hydrothermal systems by means of XRD on clay minerals (Sutri, Northern Latium, Italy). *Geothermics*, *50*, 180–188.
- De Ros, L. F. (1998). Heterogeneous generation and evolution of diagenetic quartz arenites in the Silurian-Devonian Furnas Formation of the Paraná Basin, southern Brazil. *Sedimentary Geology*, *116*, 99–128.
- Dong, T., Harris, N. B., Ayranci, K., Twemlow, C. E., & Nasichuk, B. R. (2017). The impact of composition on pore throat size and permeability in high maturity shales: Middle and Upper Devonian Horn River Group, northeastern British Columbia, Canada. *Marine and Petroleum Geology*, *81*, 220–236.
- Ehrenberg, S. N. (1991). Kaolinized, potassium-leached zones at the contacts of the Garn Formation, Haltenbanken, mid-Norwegian continental shelf. *Marine and Petroleum Geology*, *8*, 250–269.
- Folk, R. L. (1974). *Petrology of Sedimentary Rocks* (p. 184). Hemphill Publishing.
- Hanson, A. D., Ritts, B. D., & Moldowan, J. M. (2007). Organic geochemistry of oil and source rock strata of the Ordos Basin, north-central China. *AAPG Bulletin*, *91*(9), 1273–1293.
- Huang, W. B., Lu, S. F., Hersi, O. S., Wang, M., Deng, S. W., & Lu, R. J. (2017). Reservoir spaces in tight sandstones: Classification, fractal characters, and heterogeneity. *Journal of Natural Gas Science and Engineering*, *46*, 80–92.
- Hurst, A., & Nadeau, H. P. (1995). Clay microporosity in reservoir sandstones: An application of quantitative electron microscopy in petrophysical evaluation. *AAPG Bulletin*, *79*(4), 563–573.
- Jia, C. Z., Zheng, M., & Zhang, Y. F. (2012). Unconventional hydrocarbon resources in China and the prospect of exploration and development. *Petroleum Exploration and Development*, *39*(2), 139–146.
- Jiang, Z. X., Lin, S. G., Pang, X. Q., & Wang, J. (2006). The comparison of two types of tight sand gas reservoir. *Petroleum Exploration and Development*, *03*, 210–214+219. (in Chinese with English abstract).
- Lai, J., Wang, G. W., Wang, Z. Y., Chen, J., Pang, X. J., Wang, S. C., Zhou, Z. L., He, Z. B., Qin, Z. Q., & Fan, X. Q. (2018). A review on pore structure characterization in tight sandstones. *Earth-Science Reviews*, *177*, 436–457.
- Lanson, B., Beaufort, D., Berger, G., Bauer, A., Cassagnabère, A., & Meunier, A. (2002). Authigenic kaolin and illitic minerals during burial diagenesis of sandstones: A review. *Clay Minerals*, *37*(1), 1–22.
- Li, H. Y., Yue, D. L., & Zhang, X. J. (2012). Characteristics of pore structure and reservoir evaluation of low permeability reservoir in Sulige gas field. *Earth Science Frontiers*, *19*(2), 133–140.
- Li, J., Zhang, W. Z., Luo, X., & Hu, G. Y. (2008). Paleokarst reservoirs and gas accumulation in the Jingbian field, Ordos Basin. *Marine and Petroleum Geology*, *25*(4), 401–415.
- Li, P., Zheng, M., Bi, H., Wu, S. T., & Wang, X. R. (2017). Pore throat structure and fractal characteristics of tight oil sandstone: A case study in the Ordos Basin, China. *Journal of Petroleum Science and Engineering*, *149*, 665–674.
- Li, Y., Chang, X. C., Yin, W., Wang, G. W., Zhang, J. L., Shi, B. B., Zhang, J. H., & Mao, L. X. (2019). Quantitative identification of diagenetic facies and controls on reservoir quality for tight sandstones: A case study of the Triassic Chang 9 oil layer, Zhenjing area, Ordos Basin. *Marine and Petroleum Geology*, *102*, 680–694.
- Mandelbrot, B. B., Passoja, D. E., & Paullay, A. J. (1984). Fractal character of fracture surfaces of metals. *Nature*, *308*, 721–722.
- Mantovani, M., Escudero, A., & Becerro, A. I. (2010). Effect of pressure on kaolinite illitization. *Applied Clay Science*, *50*(3), 342–347.
- Martín-Martín, J. D., Gómez-Gras, D., Sanfeliu, T., Permanyer, A., Núñez, J. A., & Parcerisa, D. (2005). Conditions of kaolin illitization in the Permo-Triassic sandstones from the SE Iberian Ranges, Spain. *Journal of Geochemical Exploration*, *89*(1), 263–266.
- Mcglade, C. E., Speirs, J., & Sorrell, S. (2013). Unconventional gas—a review of regional and global resource estimates. *Energy*, *55*, 571–584.
- Morad, S., Al-Ramadan, K., Ketzer, J. M., & De Ros, L. F. (2010). The impact of diagenesis on the heterogeneity of sandstone reservoirs: A review of the role of depositional facies and sequence stratigraphy. *AAPG Bulletin*, *94*(8), 1267–1309.
- Nie, R. S., Wang, Z., Chen, Z. X., Wang, A. C., Zhou, C. H., Lei, J. Y., & Pan, Y. (2021). Stress-sensitive permeability of matrix cores and artificially fractured cores with non-proppant-filled fractures under high-pressure conditions. *Geophysics*, *86*(3), 1–102.
- Nie, R. S., Xie, F., Jia, Y. L., Jiang, K. J., Kuang, X. D., He, X. L., & Dai, L. (2016). Experimental study on the pressure-depleted flow of natural gas in a cluster of combined tight cores with a certain water saturation. *Journal of Natural Gas Science & Engineering*, *33*, 821–829.
- Ougier-Simonin, A., Renard, F., Boehm, C., & Vidal-Gilbert, S. (2016). Microfracturing and microporosity in shales. *Earth-Science Reviews*, *162*, 198–226.
- Pfeifer, P. (1984). Fractal dimension as working tool for surface-roughness problems. *Applications of Surface Science*, *18*(1–2), 146–164.
- Qiao, J. C., Zeng, J. H., Jiang, S., Feng, S., Feng, X., Guo, Z., & Teng, J. L. (2019). Heterogeneity of reservoir quality and gas accumulation in tight sandstone reservoirs revealed by pore structure characterization and physical simulation. *Fuel*, *253*, 1300–1316.
- Schlueter, E. M., Zimmerman, R. W., Witherspoon, P. A., & Cook, N. G. W. (1997). The fractal dimension of pores in

- sedimentary rocks and its influence on permeability. *Engineering Geology*, 48(3), 199–215.
- Shanley, K. W., Cluff, R. M., & Robinson, J. W. (2004). Factors controlling prolific gas production from low-permeability sandstone reservoirs: Implications for resource assessment, prospect development, and risk analysis. *AAPG Bulletin*, 88(8), 1083–1121.
- Shanley, K. W., & Cluff, R. M. (2015). The evolution of pore-scale fluid-saturation in low-permeability sandstone reservoirs. *AAPG Bulletin*, 99(10), 1957–1990.
- Sun, W. J. B., Zuo, Y. J., Wu, Z. G., Liu, H., Xi, S. J., Shui, Y., Wang, J., Liu, R. B., & Lin, J. Y. (2019). Fractal analysis of pores and the pore structure of the Lower Cambrian Niutitang shale in northern Guizhou province: Investigations using NMR, SEM and image analyses. *Marine and Petroleum Geology*, 99, 416–428.
- Wang, M., Tang, H. M., Zhao, F., Liu, S., Yang, Y., Zhang, L. H., Liao, J. J., & Lu, H. (2017). Controlling factor analysis and prediction of the quality of tight sandstone reservoirs: A case study of the He8 Member in the eastern Sulige Gas Field, Ordos Basin, China. *Journal of Natural Gas Science & Engineering*, 46, 680–698.
- Washburn, E. W. (1921). The dynamics of capillary flow. *The Physical Review*, 17, 273–283.
- Wu, J., Fan, T. L., Rivas, E. G., Gao, Z. Q., Yao, S. Q., Li, W. H., Zhang, C. J., Sun, Q. Q., Gu, Y., & Xiang, M. (2019). Impact of pore structure and fractal characteristics on the sealing capacity of Ordovician carbonate cap rock in the Tarim Basin, China. *Marine and Petroleum Geology*, 102, 557–579.
- Xoath, B. B. (1966). Coal and gas outburst. In S. Song & Y. Wang (Eds.), *Translation*. Beijing: China Industry Press.
- Yang, R., He, S., Yi, J. Z., & Hu, Q. H. (2016). Nano-scale pore structure and fractal dimension of organic-rich Wufeng-Longmaxi shale from Jiaoshiha area, Sichuan Basin: Investigations using FE-SEM, gas adsorption and helium pycnometry. *Marine and Petroleum Geology*, 70, 27–45.
- Zha, M., Wang, S., Ding, X. J., Feng, Q. H., Xue, H. T., & Su, Y. (2018). Tight oil accumulation mechanisms of the Lucaogou Formation in the Jimsar Sag, NW China: Insights from pore network modeling and physical experiments. *Journal of Asian Earth Sciences*, 178, 204–215.
- Zhang, F. D., Li, J., Li, J., Yang, S., She, Y. Q., Shao, L. Y., Guan, H., Zhu, Q. Y., & Guo, J. Y. (2017). Accumulation mechanism of tight sandstone gas in low gas generation intensity area. *Journal of Natural Gas Geoscience*, 2(2), 131–140.
- Zhou, Y., Ji, Y. L., Xu, L. M., Che, S. Q., Niu, X. B., Wan, L., Zhou, Y. Q., Li, Z. C., & You, Y. (2016). Controls on reservoir heterogeneity of tight sand oil reservoirs in Upper Triassic Yanchang Formation in Longdong area, southwest Ordos Basin, China: Implications for reservoir quality prediction and oil accumulation. *Marine and Petroleum Geology*, 78, 110–135.
- Zhu, F., Hu, W. X., Cao, J., Sun, F. N., Liu, Y. F., & Sun, Z. M. (2018). Micro/nanoscale pore structure and fractal characteristics of tight gas sandstone: A case study from the Yuanba area, northeast Sichuan Basin, China. *Marine and Petroleum Geology*, 98, 116–132.
- Zhu, S. F., Wang, X. X., Qin, Y., Jia, Y., Zhu, X. M., Zhang, J. T., & Hu, Y. Q. (2017). Occurrence and origin of pore-lining chlorite and its effectiveness on preserving porosity in sandstone of the middle Yanchang Formation in the southwest Ordos Basin. *Applied Clay Science*, 148, 25–38.
- Zhu, S. F., Zhu, X. M., Jia, Y., Cui, H., & Wang, W. Y. (2020). Diagenetic alteration, pore-throat network, and reservoir quality of tight gas sandstone reservoirs: A case study of the upper Paleozoic sequence in the northern Tianhuan depression in the Ordos Basin, China. *AAPG Bulletin*, 104(11), 2297–2324.
- Zou, C. N., Yang, Z., Tao, S. Z., Yuan, X. J., Zhu, R. K., Hou, L. H., Wu, S. T., Sun, L., Zhang, G. S., Bai, B., Wang, L., Gao, Z. L., & Pang, Z. L. (2013). Continuous hydrocarbon accumulation over a large area as a distinguishing characteristic of unconventional petroleum: The Ordos Basin, North-Central China. *Earth-Science Reviews*, 126, 358–369.